

# A comprehensive separation of dark matter and baryonic mass components in galaxy clusters II: an overview of the mass distribution in Abell S1063

Benjamin Beauchesne,<sup>1,2\*</sup> Benjamin Clément,<sup>3</sup> Marceau Limousin,<sup>4</sup> Anna Niemiec,<sup>5</sup>  
Mathilde Jauzac,<sup>1,2,6,7</sup> Belén Alcalde Pampliega,<sup>8,9,10</sup> Johan Richard,<sup>11</sup> Guillaume Mahler,<sup>12</sup> Jose M. Diego,<sup>13</sup>  
Pascale Hibon,<sup>8</sup> Anton M. Koekemoer,<sup>14</sup> Thomas Connor,<sup>15</sup> Jean-Paul Kneib,<sup>3</sup> Andreas L. Faisst<sup>16</sup>

<sup>1</sup>Centre for Extragalactic Astronomy, Department of Physics, Durham University, South Road, Durham DH1 3LE, UK

<sup>2</sup>Institute for Computational Cosmology, Department of Physics, Durham University, South Road, Durham DH1 3LE, UK

<sup>3</sup>Institute of Physics, Laboratory of Astrophysics, Ecole Polytechnique Fédérale de Lausanne (EPFL), Observatoire de Sauverny, 1290 Versoix, Switzerland

<sup>4</sup>Aix Marseille Univ, CNRS, CNES, LAM, Marseille, France

<sup>5</sup>Univ. Grenoble Alpes, CNRS, Grenoble INP, LPSC IN2P3, 53, Avenue des Martyrs, 38000 Grenoble, France

<sup>6</sup>Astrophysics Research Centre, University of KwaZulu-Natal, Westville Campus, Durban 4041, South Africa

<sup>7</sup>School of Mathematics, Statistics & Computer Science, University of KwaZulu-Natal, Westville Campus, Durban 4041, South Africa

<sup>8</sup>ESO Vitacura, Alonso de Córdova 3107, Vitacura, Casilla 19001, Santiago de Chile, Chile

<sup>9</sup>Instituto de Estudios Astrofísicos, Facultad de Ingeniería y 455 Ciencias, Universidad Diego Portales, Av. Ejército Libertador 441, Santiago, Chile

<sup>10</sup>SKA Observatory, Jodrell Bank, SK11 9FT, UK

<sup>11</sup>Univ Lyon, Univ Lyon1, Ens de Lyon, CNRS, Centre de Recherche Astrophysique de Lyon (CRAL) UMR5574, F-69230 Saint-Genis-Laval, France

<sup>12</sup>STAR Institute, Quartier Agora - Allée du six Août, 19c B-4000 Liège, Belgium

<sup>13</sup>Instituto de Física de Cantabria (CSIC-UC). Avda. Los Castros s/n. 39005 Santander, Spain

<sup>14</sup>Space Telescope Science Institute, 3700 San Martin Dr., Baltimore, MD 21218, USA

<sup>15</sup>Center for Astrophysics | Harvard & Smithsonian, 60 Garden St., Cambridge, MA 02138, USA

<sup>16</sup>Caltech/IPAC, 1200 E. California Blvd. Pasadena, CA 91125, USA

Accepted XXX. Received YYY; in original form ZZZ

## ABSTRACT

In the first paper of this series, we derived mass constraints on the total mass and the baryonic components of the galaxy cluster Abell S1063. The main focus was to recover stellar masses and kinematics for cluster members, the brightest cluster galaxy (BCG) and the intra-cluster light (ICL). In this second paper, we introduce a multi-probe mass modelling approach that incorporates constraints on both the total mass and the individual baryonic components. We obtain comprehensive mass models of Abell S1063, in which the dark matter distribution is disentangled from the baryonic mass at both cluster and galaxy scales. The best-fitting mass model achieves an RMS of 0.50'' on the multiple image positions. The kinematic profiles of the BCG & ICL, as well as the X-ray surface brightness of the intra-cluster gas, are accurately reproduced within observational uncertainties. However, a 35 km/s scatter is required for the cluster member line-of-sight dispersions. This method yields the most complex parametric mass model with consistency among almost all available mass constraints. We find a  $1\sigma$  agreement between the inferred stellar-to-subhalo mass relation and that predicted by large-scale cosmological simulations. The ICL stellar mass derived from our model is consistent with estimates from stellar population modelling. We present the first multi-probe mass modelling method capable of disentangling the dark matter from the baryonic mass distributions in massive galaxy clusters. Its results, such as the stellar-to-subhalo mass relation or the distribution of each mass component, can be directly compared to hydrodynamical cosmological simulations such as illustrisTNG.

**Key words:** gravitational lensing: strong – galaxies: clusters: general – galaxies: clusters: individual: Abell S1063 – X-rays: galaxies: clusters – Galaxy: kinematics and dynamics – Galaxy: stellar content

## 1 INTRODUCTION

In this series of two papers, we aim to develop a comprehensive mass modelling method in which each main cluster mass component

\* E-mail: benjamin.e.beauchesne@durham.ac.uk

is modelled, i.e., where dark matter (DM) is fully separated from baryons. Such a method would generate some of the most sophisticated parametric mass models to date, representing the first approach to achieve consistency across nearly all available mass probes. This new method extends the framework developed by [Beauchesne et al.](#) (hereafter B24 [2024](#)), which combines constraints from strong lensing together with the X-ray emission from the intra-cluster gas in a self-consistent framework. Thanks to this combined dataset, the intra-cluster gas or intra-cluster medium (ICM), i.e., the main contributor to the baryonic mass budget, can be disentangled from the total mass. Hence, this series of papers now focuses on the remaining baryonic component, i.e. the stellar mass, which is contained in cluster galaxies and the intra-cluster stars. The latter are responsible for emitting the intra-cluster light (ICL). As in the cluster centre, the brightest cluster galaxy (BCG) is difficult to distinguish from the ICL, we thus consider them as a single component, denoted BCG & ICL.

In [Beauchesne \(2025\)](#) (hereafter B25a), we detail the mass constraints required to set up our comprehensive mass modelling of Abell S1063 (Hereafter AS1063). In section 3, we present the existing set of constraints from strong lensing and X-rays taken from B24. In sections 4 and 5, we focus on the supplementary mass probes, i.e. cluster members and the BCG & ICL. That set of observations is the same for both components, although we apply different treatments adapted to their properties. We recover the cluster member light distribution by fitting all galaxies in the cluster field to reduce the bias due to the crowded environment. Thanks to this light model, we are able to subtract the galaxy light model to fit the BCG & ICL with a multi-Gaussian expansion (MGE). For both components, we fit their spectral energy density (SED) and their stellar kinematics to obtain stellar mass estimates as well as a total mass probe. We recall a part of the mass constraints presented in B25a, in Fig 1.

In this second paper, we now present the mass modelling methodology and detail how we use the supplementary mass constraints from B25a. In Sect. 2, we detail the mass model parametrisation of each component, where we use the light distribution from cluster members and the BCG & ICL as a tracer of their stellar mass distribution. In Sect. 3, we define the likelihoods for each mass probe: X-ray surface brightness, strong lensing systems, cluster member kinematics, and the BCG & ICL component. We conclude this section by describing the tailored optimisation process required by the complex mass model needed to accommodate all these constraints. We then present the mass model results in Sect. 4 and discuss the reliability of the mass estimates from the new component in Sect. 5.

We recall the convention used in B25a, where we adopt a flat  $\Lambda$ CDM cosmology with  $\Omega_\Lambda = 0.7$ ,  $\Omega_m = 0.3$  and  $H_0 = 70 \text{ km s}^{-1} \text{ Mpc}^{-1}$ . Magnitudes are quoted in the AB system. The uncertainties quoted in that article are the median-centred credible intervals (CI) based on the posterior distribution of the considered random variable. These intervals are presented as  $n\sigma$  CI where  $n$  is an integer such that CI contains  $100 \times \text{erf}\left(\frac{n}{\sqrt{2}}\right)$  per cent of the posterior. If we use  $\sigma$  to denote a standard deviation, we explicitly notify it in the text.

## 2 MASS MODELLING HYPOTHESES

In our model, we aim to disentangle the DM from the baryonic components at galaxy and cluster scales. In the following, we define how we model the main cluster components (DM, BCG & ICL, intra-cluster medium, and cluster members) so that their respective baryonic fractions can be assigned their own mass components.

### 2.1 Intra Cluster Medium

To model the ICM, we follow the same method as in B24, as it already fits our requirement of separating the baryonic mass from the DM. The gas distribution is modelled by a sum of dPIE potentials in a free-form way. All potentials are free to move within the cluster field, and we only fix their cut radii at 1.25 Mpc, as in B24. Indeed, it is ill-constrained when more than one potential is used. This cut radius limit corresponds to the radius at which the observed number counts are approximately at the background value.

We define the number of potentials needed by following the goodness-of-fit procedure presented in B24, which consists of adding a new potential until the resulting best-fitting model can explain properly the observed X-ray emission according to the B24 criterion. This criterion is an adaptation of the usual goodness-of-fit assessment with  $\chi^2$  1 for the X-ray likelihood defined in Sect. 3.1. Hence, as in B24, we use three dPIEs to model the hot gas in AS1063.

### 2.2 Cluster members

To reach our goal, we deviate from the standard modelling of cluster members used in the LENSTOOL software ([Kneib et al. 1993](#); [Jullo et al. 2007](#)). Instead, we develop a framework that models DM and baryons in each galaxy using individual mass profiles. We use dPIE potentials for their computational efficiency rather than combining a Sérsic and a power-law profile as it is commonly done in galaxy-scale lensing analyses (e.g. [Shajib et al. 2021](#)). However, a dPIE profile can approximate relatively well a Sérsic light profile for a Sérsic index between 1 and 4 ([Dutton et al. 2011](#)). Each galaxy component (baryons and DM) is modelled with a separate dPIE profile, with several simplifying assumptions to limit free parameters. Hence, we use the same centre coordinates, ellipticity and position angle for both dPIEs. These parameters are assumed to follow the light distribution. We fix these parameters to the best-fitting of the cluster member light profile with a dPIE presented in B25a (section 4.1). The core and cut radii of the baryonic dPIE ( $r_{\text{core,b}}$  and  $r_{\text{cut,b}}$ ), are fixed to the values of the light profile as well. Only the central velocity dispersion  $\sigma_{0,b}$  remains free, which we rescale to match the stellar mass from B25a (section 4.3). Hence, the baryonic component is fixed in the overall model and is determined only from measurements independent of the lensing analysis.

For the DM component, radii,  $r_{\text{core,DM}}$  and  $r_{\text{cut,DM}}$ , and velocity dispersion,  $\sigma_{0,DM}$ , are scaled by a spatial and concentration scale,  $\alpha_c$  and  $\beta_c$ , with respect to their baryonic counterpart, ( $r_{\text{core,b}}$ ,  $r_{\text{cut,b}}$  and  $\sigma_{0,b}$ ), such that:

$$r_{\text{core,DM}} = \alpha_c r_{\text{core,b}} \quad (1)$$

$$r_{\text{cut,DM}} = \alpha_c r_{\text{cut,b}} \quad (2)$$

$$\sigma_{0,DM} = \beta_c \sigma_{0,b} \quad (3)$$

The spatial scale,  $\alpha_c$ , is assumed to be the same for all cluster members, and is optimised with our set of heterogeneous constraints. In reality, we expect a radial cluster-centric variation of this parameter as it is linked to the tidal stripping of DM during the infall of the galaxy within the cluster potential well ([Niemic et al. 2022](#)). We leave the exploration of such variations for future work.

$\beta$  is different for each cluster member, and is recovered through the modelling of the Stellar-to-subhalo mass relation (SsHMR) in the model under the form of a double power-law as in [Niemic et al. \(2022\)](#) and [Moster et al. \(2013\)](#), such that:

$$M_{\text{tot}} = 2N \left( \left( \frac{M_*}{M_1} \right)^\delta + \left( \frac{M_*}{M_1} \right)^{-\gamma} \right) M_* \quad (4)$$

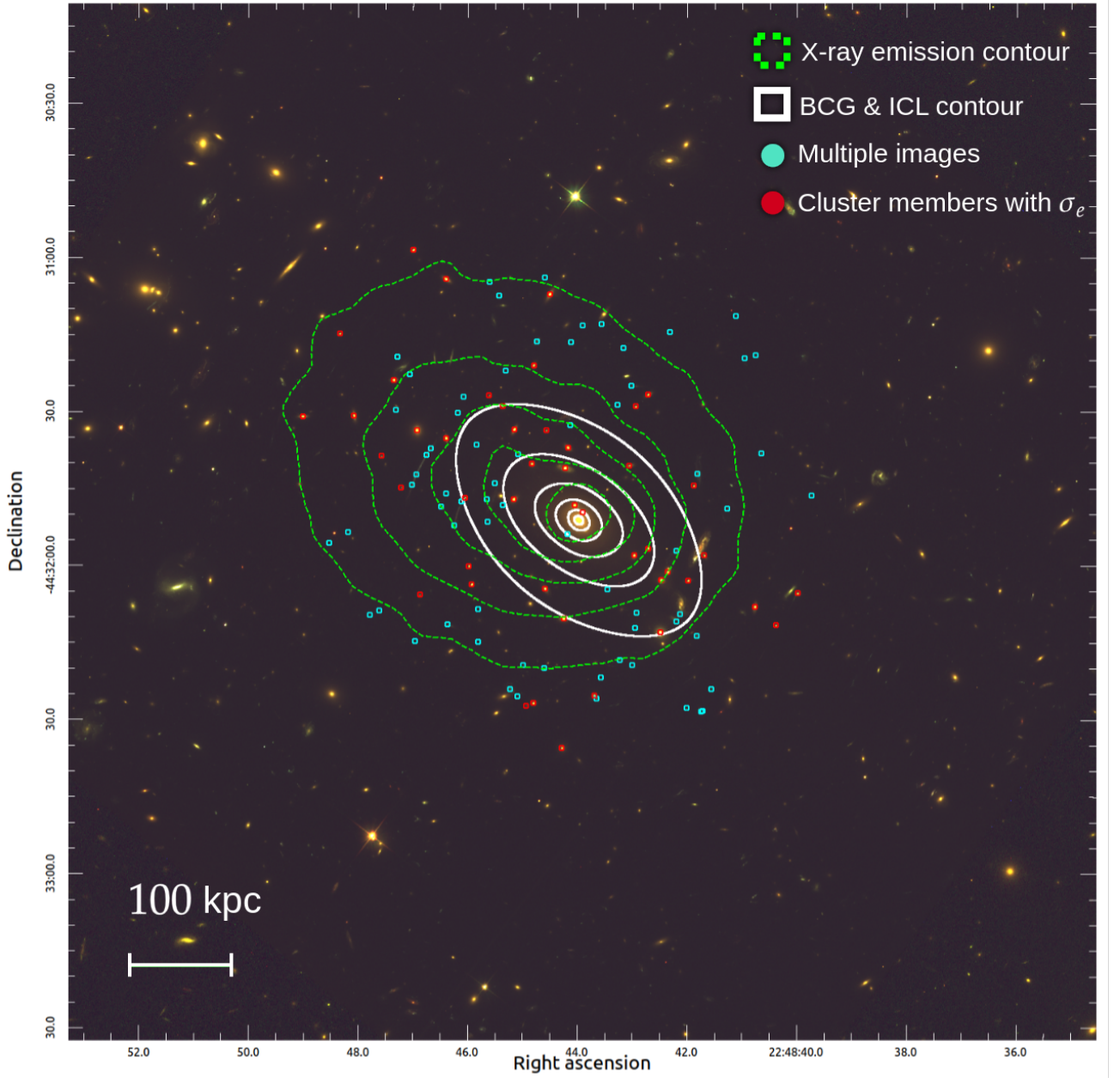


**Figure 1.** The BUFFALO colour composite image of AS1063 with the following *HST* filters: F435W (blue), F606W (green) and F814W (red). The X-ray surface brightness from the CHANDRA X-RAY OBSERVATORY is shown by the green dashed contours. The set of multiple images used in this work is highlighted by the cyan circles. The white contours present the BCG & ICL light distribution as fitted in B25a. Cluster members for which we measure the velocity dispersion,  $\sigma_e$ , in B25a are highlighted by blue circles.

Where  $N$ ,  $M_1$ ,  $\delta$  and  $\gamma$  are optimised, and define the cluster member distribution model with  $\alpha_c$ . We could switch roles between  $\alpha_c$  and  $\beta_c$ . In that case, we would optimise  $\beta_c$  and set  $\alpha_c$  with the SsHMR. However,  $\beta_c$  is more likely to be ill-constrained by strong lensing as it mostly affects cluster members inner profiles.

In our modelling, the SsHMR is the usual scaling relation used for cluster members modelling with LENSTOOL. However, instead of using an observational law, we use a parametrisation oriented toward comparison with cosmological simulations. The SsHMR of our model can be directly compared to simulation results such as the one presented in Niemiec et al. (2022). We recover  $\beta_c$  from the

SsHMR by writing the total mass of the combined dPIE models,  $M_{\text{tot}}$ , such that:

$$M_{\text{tot}} = \left( \alpha_c \beta_c^2 \frac{LM_{\odot}}{L_{\odot}} + M_{*} \right) \quad (5)$$

Where  $L$  is the total luminosity of the dPIE fitted to the light distribution, and  $M_{*}$  is the stellar mass associated with the object.

In contrast to B24, we do not inject the cluster member line-of-sight velocity dispersion (LOSVD) in their associated dPIE parameters. We would rather use them as a new set of constraints, as presented in Sect. 3.3. Hence, it allows us to include more directly

the measurement uncertainty on the LOSVD as well as to balance its information against other mass probes, such as strong lensing, within the inference process. In B24, these quantities are accounted for with the prior on the galaxy scaling law.

As in B25a (section 4.3), we obtain stellar mass estimates from different SED models used to define three different parametrisations of cluster members. Hence, we gain insights into the influence of SED systematic biases on this type of modelling, particularly on the SsHMR discussed in Sect. 5.4.

## 2.3 BCG & ICL

To model the BCG & ICL component, we assume a stellar component to represent its baryonic distribution and a DM component for the BCG. The motivation behind the BCG DM component is to allow for different mass slopes at scales differing from the main DM halo.

We model the BCG & ICL stellar component using an MGE parametrisation. We begin with the MGE model of its light distribution in the F160W filter, measured in B25a (section 5.1). Contours of the MGE model are presented in Fig. 1. We adopt identical parameters for light and mass distributions, except that the Gaussian normalisations now represent the stellar mass-to-light ratio  $\Upsilon_{*}^{\text{BCG}}$  of the BCG & ICL component. We designate the estimate of  $\Upsilon_{*}^{\text{BCG}}$  by LENSTOOL as  $\Upsilon_{*,\text{lt}}^{\text{BCG}}$ , in contrast to  $\Upsilon_{*,\text{F160W}}^{\text{BCG}}$  that we refer to as  $\Upsilon_{*,\text{SED}}^{\text{BCG}}$ . We could impose a prior on  $\Upsilon_{*,\text{lt}}^{\text{BCG}}$  based on  $\Upsilon_{*,\text{SED}}^{\text{BCG}}$  as estimated in B25a (section 5.3). However, we prefer a uniform prior since SED fits can misestimate this ratio when the assumed initial mass function (IMF) is inappropriate for the object. In particular, stellar mass estimates from kinematic modelling of early-type galaxies present significant differences compared to SED estimates (for a review on this topic see [Smith 2020](#)). To further accommodate for such discrepancies, we define three MGE parametrisations which allow for different degrees of variation of  $\Upsilon_{*}^{\text{BCG}}$  with the cluster-centric radius. The first parametrisation assumes constant  $\Upsilon_{*}^{\text{BCG}}$ , renormalising the entire light distribution with a single coefficient  $\Upsilon_{*,\text{lt}}^{\text{BCG},1}$ . We refer to this parametrisation as “BCG - ML 1”. The second uses two coefficients:  $\Upsilon_{*,\text{lt},1}^{\text{BCG},2}$  for Gaussians with standard deviations smaller than the BCG half-light radius ( $R_e = 17$  kpc; [Tortorelli et al. \(2018\)](#)), and  $\Upsilon_{*,\text{lt},2}^{\text{BCG},2}$  for wider Gaussians. This effectively separates the BCG from the ICL contributions. We refer to this parametrisation as “BCG - ML 2”. To accommodate wider variations of  $\Upsilon_{*}^{\text{BCG}}$ , we make three groups of Gaussians through a K-means clustering method as implemented in SCIKIT-LEARN ([Pedregosa et al. 2011](#)), each represented by one coefficient,  $\Upsilon_{*,\text{lt},i}^{\text{BCG},3}$  where  $i \in \{1, 2, 3\}$ .  $\Upsilon_{*,\text{lt},1}^{\text{BCG},3}$  represents the same group of Gaussians as  $\Upsilon_{*,\text{lt},1}^{\text{BCG},2}$ , while  $\Upsilon_{*,\text{lt},2}^{\text{BCG},3}$  and  $\Upsilon_{*,\text{lt},3}^{\text{BCG},3}$  allow for more variation of  $\Upsilon_{*}^{\text{BCG}}$  within the ICL. We refer to this last parametrisation as “BCG - ML 3”.

Since LENSTOOL lacks native MGE potential implementation, we incorporate them as fixed external maps of lensing quantities (computed in B25a, section 5.1) scaled by normalisation factors. When we split the MGE parametrisation into different groups, we reproduce the same procedure for each group to compute the lensing quantities as if they were separate MGE potentials. We include the map of the lensing quantities by interpolating them with degree 3 B-spline surfaces, allowing us to use the spline implementation of LENSTOOL ([Beauchesne et al. 2021](#)). In contrast to [Beauchesne et al. \(2021\)](#), we do not impose boundary conditions, and there is a different B-spline surface for each quantity: lensing potential, deflection angle, convergence and shear. We simply use the implementation to compute the value of the B-spline surface. This approach generalises to any light distribution parametrisation, accommodating complex

cases such as SMACS J0723.3-7323 ([Mahler et al. 2023](#)). We chose a MGE parametrisation specifically to enable stellar kinematic analysis through Jeans Anisotropic Modelling (JAM), which requires MGE-parametrised mass and light profiles.

To model the DM component of the BCG, we use a dPIE profile. Regarding its parameters, we fix its centre to the BCG centroid and leave the other parameters free to vary. We allow for position angle and ellipticity values which are possibly different from the light distribution. We also allow for possible offsets between DM and light distributions, as parametrised by the smooth cluster scale DM halo that we define in the following section.

## 2.4 Dark matter

For the DM cluster-scale smooth component, we use a modelling approach similar to other LENSTOOL models to represent the bulk of the cluster mass. This component is often referred as the cluster DM component by neglecting baryons contained in the ICM and the ICL. In our case, since we are modelling the baryons with other profiles, it only accounts for the DM mass.

We follow the approach of B24 by using two dPIEs haloes, one representing the main cluster DM halo, and a second one representing the North-East (NE) halo. Regarding the model parameters, we use the same assumptions as B24 for the NE halo position and radii, but we leave its position angle and ellipticity free to vary. We allow all of these parameters to vary for the main clump, and we constrain its central position to a square of 10 arcsec centred around the BCG position. Similarly to B24, we fix the cut radius to 3 Mpc.

These two additional dPIEs complete the cluster mass model. Overall, the model includes 588 different profiles. Cluster members dominate this count, with each galaxy contributing two profiles (one for baryons, one for DM). Despite the large profile count, most free parameters characterise cluster-scale components like the main DM halo and ICM, which have fewer assumptions than the cluster member population.

## 3 LIKELIHOODS

Thanks to our comprehensive model presented in Sect. 2, we can define likelihoods for our set of heterogeneous constraints: lensing, cluster members,  $\sigma_e$ , X-ray surface brightness and BCG & ICL,  $V_{\text{rms}}$ . We recall the set of constraints in Fig. 1, with X-ray surface brightness contours, multiple image systems and cluster members with measured kinematics. Each of these likelihoods constrains different parts of the model as presented in Fig. 2, where each model component is associated with different likelihoods. We have strong lensing ( $\mathcal{L}_{\text{SL}}$ ), X-rays ( $\mathcal{L}_{\text{X-ray}}$ ), cluster member kinematics ( $\mathcal{L}_{\text{CL,kin}}$ ) and the BCG & ICL kinematics ( $\mathcal{L}_{\text{BCG,kin}}$ ) likelihoods. Only the first one,  $\mathcal{L}_{\text{SL}}$ , constrains the whole mass distribution as it is sensitive to the total mass of the cluster. At the exception of  $\mathcal{L}_{\text{BCG,kin}}$  which also depends on the total mass in the cluster core, the last two,  $\mathcal{L}_{\text{X-ray}}$  and  $\mathcal{L}_{\text{CL,kin}}$ , only constrain one model component each. We define each of these likelihoods in the following sections. In Sect. 3.5, we detail our parameter inference procedure.

### 3.1 X-ray surface brightness

To allow our model to account for the ICM X-ray emission as a constraint, we use the mass distribution of the dPIEs associated with the gas to predict the cluster X-ray surface brightness. We use the same transformation as in B24 to convert the gas mass distribution

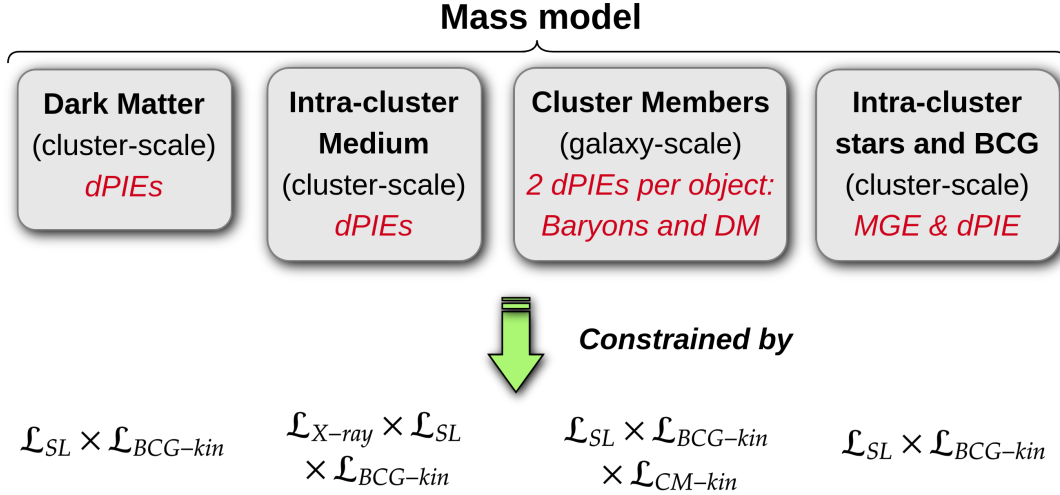


**Figure 2.** Overview of each model component. Each one of them is associated with a set of analytical profiles and the likelihood that they are affecting.

to its associated electron density, and then its surface brightness. We refer the reader to B24 and the references within for a detailed procedure description.

To define the likelihood and to take into account the limitations of our modelling choices, we incorporate an intrinsic error on the X-ray photon count,  $\sigma_X$ , and we use a likelihood based on the Negative Binomial distribution ( $\mathbb{NB}(r = \mu_i^2/\sigma_X^2, p = \mu_i/(\mu_i + \sigma_X^2))$  with  $\mu_i$  the expected photon count in a bin). The full likelihood is then defined as follows:

$$\mathcal{L}_{X-ray} = \prod_i \frac{\Gamma(k_i + \frac{\mu_i^2}{\sigma_X^2})}{k_i! \Gamma(\frac{\mu_i^2}{\sigma_X^2})} \left( \frac{\mu_i}{\mu_i + \sigma_X^2} \right)^{\frac{\mu_i^2}{\sigma_X^2}} \left( \frac{\sigma_X^2}{\mu_i + \sigma_X^2} \right)^{k_i} \quad (6)$$

Where  $\mu_i$  is the expected photon counts from the model in each pixel of the map,  $k_i$  is the observed number of photon counts in a bin, and  $\Gamma$  represents the well-known gamma function.

In contrast to B24, we do not use a constant value of  $\sigma_X^2$  for the whole field of AS1063. We use an intrinsic error proportional to the expected value of the surface brightness model, such that  $\sigma_X = a\mu_i$ , where  $a$  is the error parameter to optimise. It is more adapted to the motivation behind the addition of this error. B24 motivated the addition of  $\sigma_X^2$  to account for the model limitations in reproducing gas mass variations below the cluster-scale. The gas sloshing pattern identified in B24 is an example of such variations. Hence, we expect such phenomena to have an amplitude correlated to the gas density as reflected by the expression of  $\sigma_X$ . If a constant error is still needed, it would likely indicate a misestimation of the background sky.

### 3.2 Multiple images positions

For the strong lensing constraints, we also follow the same definition as in B24, particularly in choosing the source position of each multiply-imaged system. Indeed, we do not rely on a weighted barycenter of the positions of each image in the source plane but rather use it as a starting point that we optimise to find the best-available source position for a given system. We assume that the uncertainties on the positions of multiply-imaged systems are well

represented by independent Gaussian distributions, which gives the following likelihood definition:

$$\mathcal{L}_{SL} = \prod_j \frac{1}{\prod_i^{N_{im,j}} \sigma_{ij} \sqrt{2\pi}} \exp(-\chi_j^2/2) \quad (7)$$

with  $N_{sys}$ , the total number of multiply-imaged systems,  $N_{im,j}$ , the number of images in the  $j^{th}$  system, and  $\sigma_{ij}$ , the observational error on the  $i^{th}$  images of the  $j^{th}$  system.  $\chi_j^2$  is the  $\chi^2$  statistics associated with the  $j^{th}$  system and reads as follows:

$$\chi_j^2 = \sum_i^{N_{im,j}} \frac{\|\tilde{\theta}_{i,j}^{obs} - \tilde{\theta}_{i,j}^{pred}\|^2}{\sigma_{ij}^2} \quad (8)$$

To consider the uncertainties in identifying image positions and the systematic limitation of our modelling, we use an observational error on the position of 0.55 arcsec. We select this value based on a maximum likelihood estimate to account for both observational and systematic errors such that the best-fitting model reaches a reduced  $\chi^2$  of approximately 1.

### 3.3 Cluster member kinematics

Thanks to our detailed cluster members modelling, we can access both their light and mass distributions in terms of dPIEs. We use a similar approach as in B24 to model cluster member LOSVD at the half-light radius,  $\sigma_e$ , from the light and mass distributions. The main difference is that we do not try to obtain  $\sigma_0$  from  $\sigma_e$ , but  $\sigma_e$  as a function of dPIEs parameters.

Following Beauchesne et al. (2024); Bergamini et al. (2019), the LOSVD,  $\sigma_{LOS}$ , is expressed as follows:

$$\sigma_{LOS}^2(R) = \frac{2G}{I(R)} \int_R^\infty \nu(r) M_{3D}(r) \mathcal{F}(r) r^2 \beta_{aniso}^{-2} dr \quad (9)$$

Where  $I$  and  $\nu$  are the surface density and density of the luminosity distribution, respectively.  $M_{3D}$  is the total mass enclosed in a sphere of radius  $r$ . It leaves us with two terms,  $\mathcal{F}$  and  $\beta_{aniso}$ , which are linked to the anisotropy of stars' orbits. For simplicity, we assume that these

orbits are isotropic, which gives the following formulas (Cappellari 2008):

$$\mathcal{F}(r) = \sqrt{r^2 - R^2} \text{ and } \beta_{\text{aniso}} = 0 \quad (10)$$

To match the actual measurements of  $\sigma_{\text{ap}}$  and their extraction apertures,  $\sigma_{\text{LOS}}$  is averaged in circular apertures of radius  $R'$ . We obtain the following expression:

$$\sigma_{\text{ap}}^2(R') = \frac{2\pi}{L(R')} \int_0^{R'} \sigma_{\text{LOS}}^2(R) I(R) R dR \quad (11)$$

Where  $L(R')$  is the luminosity enclosed in a circle of radius  $R'$ . In our case, we have three dPIEs, one for the light ( $\sigma_{0,l}, r_{\text{core},l}, r_{\text{cut},l}$ ), one for the baryons ( $\sigma_{0,b}, r_{\text{core},b}, r_{\text{cut},b}$ ) and one for DM ( $\sigma_{0,\text{DM}}, r_{\text{core},\text{DM}}, r_{\text{cut},\text{DM}}$ ) masses. We assume that the mass and light of the considered cluster members are the only components that significantly affect the LOSVD. Thus, we obtain the following expressions for the different terms presented in the previous equations:

$$\nu(r) = \frac{\sigma_{0,l}^2(r_{\text{core},l} + r_{\text{cut},l})}{2Y_{\odot}\pi G r_{\text{core},l}^2 r_{\text{cut},l}} \frac{1}{\left(1 + \left(\frac{r}{r_{\text{core},l}}\right)^2\right) \left(1 + \left(\frac{r}{r_{\text{cut},l}}\right)^2\right)} \quad (12)$$

$$I(r) = \frac{2\sigma_{0,l}^2 r_{\text{cut},l}}{G(r_{\text{cut},l} - r_{\text{core},l})} Y_{\odot} \left( \frac{1}{\sqrt{r^2 + r_{\text{core},l}^2}} - \frac{1}{\sqrt{r^2 + r_{\text{cut},l}^2}} \right) \quad (13)$$

$$M_{3D}(r) = \sum_{i \in \{b, \text{DM}\}} \left( \frac{2\sigma_{0,i}^2 r_{\text{cut},i}}{G(r_{\text{cut},i} - r_{\text{core},i})} \times \right. \quad (14)$$

$$\left. \left( r_{\text{cut},i} \arctan\left(\frac{r}{r_{\text{cut},i}}\right) - r_{\text{core},i} \arctan\left(\frac{r}{r_{\text{core},i}}\right) \right) \right) \quad (15)$$

$$L(r) = \frac{2\sigma_{0,l}^2 r_{\text{cut},l}}{G(r_{\text{cut},l} - r_{\text{core},l})} Y_{\odot} \times \quad (16)$$

$$\left( \sqrt{r^2 + r_{\text{core},l}^2} + r_{\text{cut},l} - \sqrt{r^2 + r_{\text{cut},l}^2} - r_{\text{core},l} \right) \quad (17)$$

In our case, we extract the LOSVD in a radius equal to the half-light radius of the considered cluster member, which in the case of the dPIE is (Elíasdóttir et al. 2007):

$$R_e = \frac{3}{4} \sqrt{r_{\text{core},l}^2 + \frac{10}{3} r_{\text{core},l} r_{\text{cut},l} + r_{\text{cut},l}^2} \quad (18)$$

We have now settled everything to compute  $\sigma_e = \sigma_{\text{ap}}(R_e)$ , and define the likelihood associated with cluster member kinematics,  $\mathcal{L}_{\text{CM-kin}}$ . We assume that each  $\sigma_e$  measurement is well-represented by a Gaussian distribution, which gives the following definition:

$$\mathcal{L}_{\text{CM-kin}} = \prod_j^{N_{\text{gal}}} \frac{1}{\delta_{\sigma_{e,i}} \sqrt{2\pi}} \exp\left(-\frac{(\sigma_{e,i} - \sigma_{e,\text{model},i})^2}{2\delta_{\sigma_{e,i}}^2}\right) \quad (19)$$

Where  $N_{\text{gal}}$  is the number of cluster members with a measured LOSVD, and  $\delta_{\sigma_{e,i}}$  is the observational error on that measurement.  $\sigma_{e,i}$  and  $\sigma_{e,\text{model},i}$  are the values of the measured and model-predicted LOSVD, respectively.

As our model parametrisation includes several hypotheses to simplify the model, we cannot reproduce each LOSVD within its error bars. Similarly to the lensing constraints, we add an intrinsic error, such that the associated reduced  $\chi^2$  is approximately 1 for the mode of the posterior. We estimate the systematic error to be of 35 km/s from a preliminary estimate of the maximum likelihood.

### 3.4 BCG & ICL kinematics

To model the kinematics of the BCG & ICL, we rely on JAM to obtain a 2D model and the JAMPY package (Cappellari 2008). We already have an axisymmetric MGE representation of the light distribution as measured in B25a (section 4.1). Thus, we need to define a similar representation for the mass so we can compute the JAM kinematic model. To be computationally efficient, we base the mass model on the 1D mass profile of the galaxy cluster. We compute the averaged mass density in spherical shells that we fit with a 1D MGE representation. We include all profiles that define cluster-scale distributions, such as the smooth DM, the gas and the BCG & ICL components, in the mass density. In preliminary tests, we find that adding some cluster members is necessary to account for all the mass required by the stellar kinematics. Hence, we include each cluster member located in the extraction area of the kinematics. This selection is correct under the assumption of a single mass plane, although in reality, we may include cluster members that would not be in the spherical shells used to estimate the 1D mass profile. We build the 2D MGE mass by assuming the same position angle as the light distribution. This is required by the JAM method. To estimate an ellipticity as close as possible to the underlying mass distribution, we uniformly sample points in the combined area of all extraction regions of the kinematics. We compute the second moment of the mass distribution in the  $x$  and  $y$  axes of the LENSTOOL reference frame and estimate the ellipticity with the same formulae as SEXTRACTOR<sup>1</sup>. In preliminary tests, we tried to use the 2D mass density and obtain the 2D MGE representation directly. However, the requirement of having the same position angle led to a bad fit of the mass by the 2D MGE.

With a representation of the light and mass under the form of MGEs, we need to define some specific parameters of the JAM method to define the kinematic model properly. These parameters are the inclination with respect to the LOS, and the anisotropy of the stars' orbits. We marginalise on the inclination by uniformly sampling it in the range that leads to a viable kinematic model. We define the minimal inclination,  $\theta_{\text{min}}$ , with the following equation from the JAM code parameter restriction:

$$q_{\text{obs,min}} = \sqrt{\cos^2(\theta_{\text{min}}) + q_{\text{min}} \sin^2(\theta_{\text{min}})} \quad (20)$$

Where  $q_{\text{obs,min}}$  is the minimal axis ratio among the Gaussians of both MGE representations (i.e. light and mass), and  $q_{\text{min}}$  is the minimal axis ratio of the deprojected Gaussians in 3D. As in the JAM code, we fix  $q_{\text{min}}$  to 0.05.  $\theta_{\text{max}} = 90$  degree represents the edge-on case. In the JAM code, there are multiple choices for the anisotropy of the stars' orbits: cylindrical alignment of the velocity ellipsoid (Cappellari 2008), spherical alignment (Cappellari 2020) and custom functions such as a logistic (Simon et al. 2024) or a constant function. In the preliminary test, we found no significant difference between the two types of alignment when integrating the kinematic model in the observational bins. We try to use a logistic function as in Simon et al. (2024) to constrain the anisotropy with the data. We use a gradient descent method to optimise the anisotropy at a constant mass model, but the parameters were ill-constrained and stayed around the starting points. Hence, we use the cylindrical alignment as it is a less costly computation than the spherical one. Once the JAM 2D model is defined in the area where the  $V_{\text{rms}}$  is measured, we integrate the model in the elliptical annuli used for the extraction with a trapezoid method.

<sup>1</sup> <https://sextractor.readthedocs.io/en/latest/Position.html>

In the observation bins, we then define the BCG & ICL kinematics likelihood  $\mathcal{L}_{\text{BCG-kin}}$  as a Gaussian likelihood on the  $V_{\text{rms}}$  measurements such that:

$$\mathcal{L}_{\text{CM-kin}} = \prod_j^{N_{\text{bin}}} \frac{1}{\delta V_{\text{rms},i} \sqrt{2\pi}} \exp \left( -\frac{(V_{\text{rms},i} - V_{\text{rms},i}^{\text{model}})^2}{2\delta V_{\text{rms},i}^2} \right) \quad (21)$$

where  $N_{\text{bin}}$  is the number of extraction bins where  $V_{\text{rms},i}$  has been measured with the observational error  $\delta V_{\text{rms},i}$ .  $V_{\text{rms},i}^{\text{model}}$  is the model predicted LOS velocity moment.

### 3.5 Optimisation process

In the case of our modelling, the computational cost of the combined likelihood is too high to use regular sampling methods of the posterior, such as Markov Chain Monte Carlo or Nested sampling. However, this cost begins to be too expensive only when we consider the kinematic model of the BCG & ICL. Indeed, this likelihood only constrains some of the parameters of the model, and the convergence depends on the whole likelihood.

The BCG & ICL kinematics are particularly interesting as they complete the strong lensing constraints in the cluster core. Hence, we do not want to exclude them. We converge on the optimisation process presented in Fig. 3, which uses an approximation to obtain the posterior of the total likelihood. We start the inference scheme by running a regular sampling method to obtain the posterior of the incomplete likelihood  $\mathcal{L}_{\text{CM-kin}} \times \mathcal{L}_{\text{SL}} \times \mathcal{L}_{\text{X-ray}}$ . In our case, we rely on the nested sampling Monte Carlo algorithm, MLFRIENDS (Buchner et al. 2014; Buchner 2019) implemented in the Python package ULTRANEST<sup>2</sup> (Buchner 2021). We then consider this posterior as a biased distribution in the context of importance sampling. We aim to obtain an approximation of the posterior defined by our total likelihood, which is the target distribution for the importance sampling. In that case, we can determine the importance weight,  $w$ , as follows:

$$w \propto \frac{\mathcal{L}_{\text{CM-kin}} \times \mathcal{L}_{\text{SL}} \times \mathcal{L}_{\text{X-ray}} \times \mathcal{L}_{\text{BCG-kin}}}{\mathcal{L}_{\text{CM-kin}} \times \mathcal{L}_{\text{SL}} \times \mathcal{L}_{\text{X-ray}}} \frac{P(\theta)}{P(\theta)} \quad (22)$$

$$\propto \mathcal{L}_{\text{BCG-kin}} \quad (23)$$

Where  $P(\theta)$  represents the priors of the whole model parameters. As we can see, the importance weights vastly simplify in our case, such that they are only proportional to  $\mathcal{L}_{\text{BCG-kin}}$ . We then use the systematic resampling algorithm presented in Hol et al. (2006) to obtain our approximated posterior.

We note that such a procedure works only if the biased and target posteriors are not too different, such that the resampling keeps a maximal number of samples from the biased posterior sample. We address this issue in our case in Sect. 4.2.4, where we present the resulting posterior on the kinematic model of the BCG & ICL.

Due to the complexity of the current model, particularly the number of dPIE potentials, we have to speed up the first inference step further. Due to the limitations in multi-threading/processing of the Bayesian inference code presented above, the first step would need approximately a month on 60 CPU cores spread over several computing nodes. Hence, we use a particle swarm optimiser (Bonyadi & Michalewicz 2017) to obtain a maximum likelihood estimate and a sample of models. From this set of points, we model the likelihood with a multivariate normal distribution where we fix the mean to the best fit and scale the log-likelihood such that the true and surrogate

**Table 1.** Widely applicable information criterion (WAIC) for the different BCG & ICL parametrisations and estimation of the cluster member stellar masses with their associated root mean squared error (RMS) on the multiple image positions. We highlight in bold the two models favoured by the WAIC.

BCG model	SED cluster member	WAIC mean $\pm$ std	RMS (")
BCG - ML 1	LePHARE	$-33538.94 \pm 0.65$	0.50"
BCG - ML 1	Delayed	$-33548.34 \pm 1.47$	0.54"
BCG - ML 1	Dbl. power-law	$-33536.99 \pm 1.05$	0.50"
<b>BCG - ML 2</b>	<b>lePhare</b>	<b><math>-33523.08 \pm 1.10</math></b>	<b>0.50"</b>
<b>BCG - ML 2</b>	<b>Delayed</b>	<b><math>-33521.41 \pm 1.42</math></b>	<b>0.50"</b>
BCG - ML 2	Dbl. power-law	$-33553.69 \pm 1.86$	0.51"
BCG - ML 3	LePHARE	$-33552.96 \pm 1.75$	0.53"
BCG - ML 3	Delayed	$-33554.16 \pm 1.87$	0.54"
BCG - ML 3	Dbl. power-law	$-33544.20 \pm 1.48$	0.53"

likelihood have the same value at the best-fitting point. We sample the posterior of the surrogate likelihood and estimate a 1D posterior of each parameter with a Gaussian kernel density estimator (KDE). We ensure that the cumulative distribution function (cdf) of the Gaussian KDE encompasses the whole prior by constraining the cdf to be 0 and 1 at the lower and higher bounds of the prior. We use these 1D Gaussian KDE estimations as priors for the ULTRANEST run.

Thanks to this process, we can perform the first step of the inference in 4 to 5 days, including the particle swarm optimiser, the estimation of the approximated prior and the nested sampling run with the true likelihood. In particular, it can bias the estimation of the Bayesian evidence (i.e. marginal likelihood) of the nested sampling run. However, it is not usable in our case as we miss  $\mathcal{L}_{\text{BCG-kin}}$  from its computation. We rely on nested sampling for its robustness in finding the mode of the posterior distribution and not the marginal likelihood estimate. To ensure that this process does not bias the posterior, we provide in Appendix A the density plots of the approximated posterior from the surrogate, the posterior from the nested sampling run and the approximated posterior obtained via the final importance sampling step.

A possible issue with the importance sampling step is the under-sampling of the true posterior. Such a case happens when a small number of samples have a non-negligible weight. In particular, the value of the inclination relative to the plane of the sky influences the resulting mass models. In the case of large ellipticities (i.e.  $A/B \gtrsim 2.0$  with  $A$  and  $B$  the major and minor axis sizes), different inclinations can have a  $V_{\text{rms}}$  difference of more than 20 km/s. Such differences are enough for a set of parameters from the mass model to be located outside of the final posterior. A solution to avoid undersampling is to increase the sampling of the inclination relative to the mass models. Hence, we are sampling 3 different inclinations for each mass model.

## 4 RESULTS

### 4.1 Model discrimination

As we defined three parametrisations for the BCG & ICL mass components (Sect. 2.3) and three estimates of cluster member stellar masses (B25a, section 4.3), we produce 9 models combining each possibility. To distinguish between them, we rely on the Widely Applicable Information Criterion (WAIC) (Watanabe 2010), which uses the posterior distribution to compute the criterion value. It is quite

<sup>2</sup> <https://johannesbuchner.github.io/UltraNest/>

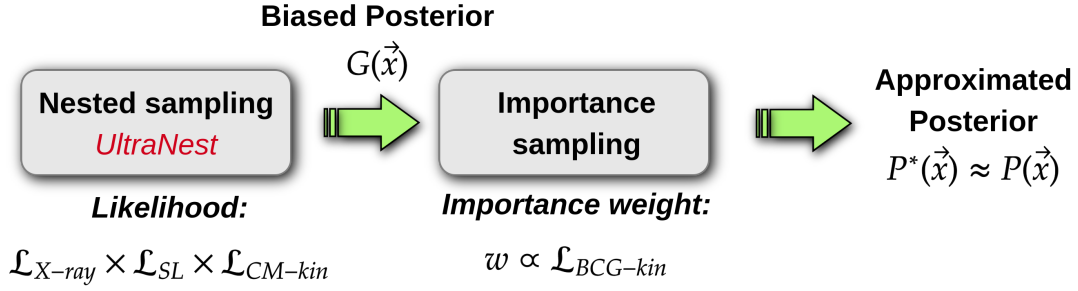


**Figure 3.** Diagram of the inference workflow in two steps. A biased posterior distribution is obtained on the combined likelihood excluding the BCG & ICL kinematics. In the second step, we resample the biased posterior through importance sampling to obtain the final posterior estimate.

similar to the Bayesian Information Criterion (BIC Schwarz 1978) or Akaike Information Criterion (AIC Akaike 1998), and is a readaptation of such criteria in a Bayesian inference context. It replaces the estimate of the maximum likelihood by its average over the posterior distribution, and the number of parameters is switched to an effective number of parameters instead. The number of effective parameters is also estimated from the parameters posterior distribution.

Table 1 presents the WAIC estimate performed for each model through the implementation in the ArviZ library (Kumar et al. 2019). We estimate the mean and standard deviation of the WAIC by randomly selecting 1000 models from the posterior, and repeating the operation 1000 times. Focusing on the BCG & ICL parametrisation, “BCG - ML 2” models are the best-performing models when averaging over the cluster member SED estimates. They are followed by the “BCG - ML 1” models and then the “BCG - ML 3” models. Except for the model with a double power-law SFH and “BCG - ML 2” parametrisation, there is an improvement at a fixed specific SED model from a model with a “BCG - ML 3” to a “BCG - ML 1” and from “BCG - ML 1” to “BCG - ML 2” parametrisation. Hence, according to the WAIC and our set of constraints, the best parametrisation of the BCG & ICL component is to assume different stellar-mass-to-light ratios for the BCG and the ICL. Providing further freedom to the varying  $Y_{*}^{\text{BCG}}$  does not improve the models, and the last coefficient,  $Y_{*,\text{It}3}^{\text{BCG},3}$ , is not constrained.

Regarding cluster member stellar masses, there is no clear preference for one SED model that would perform better for each BCG & ICL parametrisation. The SED model from LePHARE is the best, on average, among all BCG & ICL parametrisation. Although, models with LePHARE do not outperform the other models with the same BCG & ICL parametrisation. For “BCG - ML 2” parametrisation, it is equally favoured by the WAIC as the model with a delayed SFH, while for “BCG - ML 1” and “BCG - ML 3” parametrisations, it is the double power-law SFH model that has the best WAIC. In contrast to the BCG & ICL parametrisation, which can provide a significant increase in the WAIC for most SED models, these cluster member parametrisations have a smaller effect on the overall models and constraints reproduction. Another way to distinguish between these SED models would be to test their prediction of  $Y_{*}^{\text{BCG}}$  after selecting the best BCG & ICL parametrisation. This aspect is discussed in Sect. 5.1, together with the biases on  $Y_{*}^{\text{BCG}}$ . Focusing on models with a “BCG - ML 2” parametrisation, the Delayed SFH and LePHARE SED models are the two best models according to the WAIC. The uncertainties on their WAICs are too large to allow us to discriminate between them. To simplify the discussion and focus on a single model, we present the mass distribution results on the Delayed SFH model in the following sections as it has the best best-fitting models

among all. We provide the posteriors and  $1\sigma$  CI for all models with a “BCG - ML 2” parametrisations in Appendix A.

As shown in Table 1, the root mean squared error (RMS) on the multiple image positions is similar among all models. We observe the same behaviour for X-ray and the cluster member likelihood values, which are of a similar order for all models. The most impactful likelihood in the WAIC results is the BCG & ICL ones, which account for most of the combined likelihood difference between each model. As this likelihood particularly constrains the BCG & ICL component, it explains why we can discriminate between its parametrisations but not the cluster member one.

## 4.2 Reproduction of the constraints

In this section, we present how the selected mass model (i.e. Delayed SFH and “BCG - ML 2”) reproduces the constraints on each dataset. We start with lensing and X-rays in Sect. 4.2.1 and 4.2.2, respectively. We finish with the two new datasets, i.e. the BCG & ICL and cluster member stellar kinematics, in Sect. 4.2.4 and 4.2.3, respectively.

### 4.2.1 Lensing

Our best model, which uses the “BCG - ML 2” parametrisation and the SED model with a delayed SFH, has achieved a RMS of 0.50 arcsec. This is close to the RMS achieved by the other tested models. In comparison, our worst model according to the WAIC (i.e. “BCG - ML 3” parametrisation and SED model with a delayed SFH) has a RMS of 0.54 arcsec. Hence, lensing constraints are not the dominant dataset to distinguish between the models presented here, as they all perform equivalently. As we use the same set of images as B24, it is the closest comparison we can make with pre-existing models. In that case, the B24 model without a B-spline perturbation achieves an RMS of 0.60 arcsec, which highlights that we improve the reproduction of the lensing constraints with our new treatment of the BCG & ICL and cluster members. Our present model has a higher RMS than the B24 model with a B-spline perturbation, although both are close, as they have an RMS of 0.44 arcsec. We did not try to include such a component here as the B-spline perturbation as defined in Beauchesne et al. (2021) are only defined on projected quantities in the plane of the sky, although the BCG & ICL stellar kinematics require the definition of a deprojection in 3D space.

Interestingly, AS1063 has a multiply imaged system with a central image close to the BCG (Balestra et al. 2013), which is more sensitive to the BCG & ICL baryons than other systems. On that specific model, the system RMS is of 0.26 arcsec, way lower than the overall RMS and the central image has an error of 0.23 arcsec. In comparison,

B24 model had a RMS of 0.50 arcsec for that system and 0.51 arcsec for the central image. This system is a good argument in favour of our modelling approach.

#### 4.2.2 X-rays

The mass model of the intra-cluster gas is almost identical to the model obtained in B24. The two parametrisations of the likelihood intrinsic error lead to similar likelihood values with  $\mathcal{L}_{X\text{-ray}}$  of  $-33201$  for our best-fitting model, compared to  $-33189$  in B24. The log-likelihood distribution among the pixels is also close, though with the new error parametrisation, it is slightly wider, with a few pixels with worse and better likelihoods. Hence, we can estimate that the addition of the other likelihoods has not affected the estimate of the gas distribution as presented in B24.

#### 4.2.3 Cluster member kinematics

Fig. 4 presents the model-predicted velocity dispersion  $\sigma_e$  as a function of the observational measurements. To appreciate the variation due to the SED model, we provide the results for each model with the “BCG - ML 2” parametrisation and their combined results. Each mass model presents similar results in terms of scatter and uncertainties, although there are some significant differences for some galaxies depending on the SED model. This result is reflected by the reduced  $\chi^2$  of the best-fitting model of each mass modelling that varies from 0.92 to 1.05 between these three models with an assumed scatter of 35 km/s.

According to the bottom right panel of Fig. 4, systematic errors dominate the  $\sigma_e$  estimates. In particular, the bias due to the SED model is sufficient to largely dominate statistical uncertainties from the model posterior. This systematic uncertainty seems to be correlated with increasing values of  $\sigma_e$ , as points with  $\sigma_e > 200$  km/s present larger error bars. To assess such a correlation, we analyse this data set with a Spearman correlation (Spearman 1904) based on  $\sigma_e$  and  $\delta_{e,\text{sys}}/\sigma_e$ , with  $\delta_{e,\text{sys}}$  being half of the width of the  $1\sigma$  CI. We report a slight anti-correlation of  $-0.15$  with a large p-value of 0.30, rejecting a possible correlation. The same test as with  $\sigma_e$  and  $\delta_{e,\text{sys}}$  gives a correlation coefficient of 0.87, with p-values inferior to  $10^{-14}$ . Hence, the amplitude of systematic error seems to correlate with the accessible mass range for a cluster member within our parametrisation.

#### 4.2.4 BCG & ICL kinematics

Fig. 5 presents the kinematic model of the BCG & ICL component through its  $V_{\text{rms}}$ . As shown by the cyan distribution, mass models are already in good agreement with the observed stellar kinematics even when not fitted to those data. This agreement is a necessary condition to validate the importance sampling procedure, but it also increases confidence in the mass model parameterisation. Indeed, as the inner mass model is driven by prior assumptions on the mass profile, it could have deviated from the true mass without direct constraints. Thanks to the importance sampling procedure, we can significantly reduce the width of the kinematic posterior, particularly in the BCG and its vicinity, as highlighted by the dashed black line representing the BCG half-light radius.

When looking more closely at the reduced  $\chi^2$  of each model in the resampled posterior, we obtain a value of  $3.86^{+0.33}_{-0.23}$  for its  $1\sigma$  CI with a minimum of 3.40, while the best-fitting model among all datasets reaches a reduced  $\chi^2$  of 4.50. More precisely, the median distance

to the data points from the model is below 2 standard deviations for every point, except the fifth and sixth ones, which are at 2.90 and 3.82, respectively. As these two points deviate from the trend adopted by the other data points, their uncertainties are likely not accounting for some systematic biases. If we exclude them, we obtain  $3.35^{+0.51}_{-0.43}$  for the reduced  $\chi^2$   $1\sigma$  CI with a minimum at 2.34. If our kinematic model posterior agrees with the observed data, it does not include a model that agrees with the measurement uncertainties. It may highlight a limitation of our kinematic modelling or an undersampling of the posterior due to our two-step optimisation procedure.

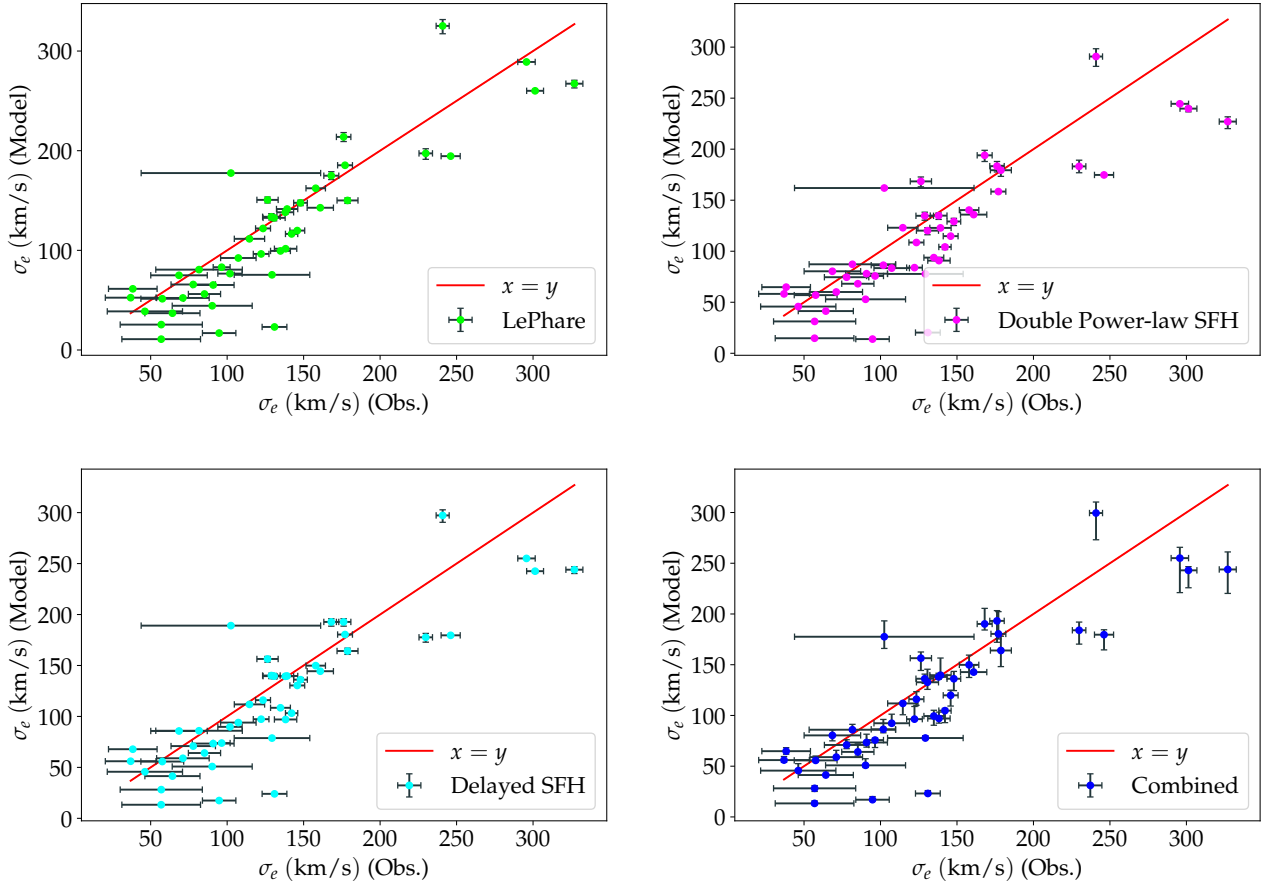
### 4.3 Mass distribution and profiles

Fig. 6 presents the normalised surface mass density or convergence of the mass model. Each cluster-scale mass component is highlighted by dashed contours. Thanks to our highly detailed mass modelling, we can disentangle each mass component. Similarly to B24, we observe a discrepancy between the intra-cluster gas and DM. The gas distribution presents a smaller ellipticity and an asymmetry toward the NE halo. It highlights the importance of considering the gas, even in the case of slowly perturbed clusters. Regarding the BCG & ICL baryons, their contribution is negligible compared to the gas and DM, except in the vicinity of the BCG. However, within a few kpc of the cluster centre, the ellipticity of the BCG & ICL highest surface mass density contour closely matches that of the DM. Moving inward, the two innermost contours of the BCG & ICL show progressively lower ellipticities, indicating a systematic deviation from the DM ellipticity toward the BCG one.

Overall, the mass distribution is globally similar to B24 and other lensing studies on AS1063 (Bergamini et al. 2019; Granata et al. 2022; Limousin et al. 2022), where the mass distribution is mostly unimodal with an asymmetry toward the NE halo. As found in B24, it is likely the remnant of a small cluster/group of galaxies infalling in AS1063. Such an event induces a gas sloshing that was confirmed by a specific pattern in the gas properties.

Fig. 7 presents the surface mass density profile of each cluster-scale component with the total mass in the left panel, and the component profiles relative to the total mass in the right panel. As we focus on the cluster scale mass distribution, DM or baryons profiles do not include the contribution from cluster members besides the BCG, although they are included in the total mass distribution. Thanks to our detailed modelling, we have access to the baryonic fraction and the contribution to each baryonic component. We can see that they reach a maximum of  $\approx 40$  per cent within the BCG, where the baryons are dominated by the BCG & ICL stellar masses. Beyond a radius of 20 kpc, the ICM becomes the dominant baryonic component, having reached the contribution of the BCG & ICL at that radius, each accounting for 7 per cent of the overall mass. The bulk of the baryonic mass in the form of ICM gas represents  $\approx 10$  per cent of the total mass up to the end of the strong lensing region at  $\approx 250$  kpc.

Our mass profile also presents reduced statistical uncertainties in comparison to B24 results. Within the strong lensing area ( $R < 250$  kpc), our total mass profile presents a  $1\sigma$  CI of  $1.30^{+0.44}_{-0.35}$  per cent of error among the considered radial bins. It represents a 28 per cent reduction compared to the same measurement from the B24 model, which has a  $1\sigma$  CI of  $1.82^{+1.06}_{-0.58}$ . Similar error reductions are observed within the BCG and its close surroundings for  $R < 30$  kpc. We obtain  $3.18^{+0.69}_{-0.50}$  and  $4.06^{+3.87}_{-1.39}$  for our model and B24’s one, respectively. In addition to the significant error reduction of the median, the width of the  $1\sigma$  CI has been divided by a factor  $\approx 4$ , highlighting the benefit of the BCG stellar kinematics constraints. Thanks to these reduced



**Figure 4.** Model predicted  $\sigma_e$  as a function of the observed one, for each SED model. The uncertainties for the observed  $\sigma_e$  are the measurement standard deviations. For the model predicted  $\sigma_e$ , the uncertainties show the  $1\sigma$  CI from the mass model posterior. The *top left*, *top right* and *bottom left* panels present the results from the mass model with LePHARE, the double power-law SFH and the delayed SFH SED models, respectively. The *bottom right* panel combines the prediction from each of these three mass models.

uncertainties, we obtain an error of  $2.10^{+1.11}_{-0.47}$  and  $4.28^{+0.18}_{-0.25}$  per cent for  $R < 250$  kpc and  $R < 30$  kpc, respectively, for the DM-only profiles.

To complete the picture of the mass profiles, we present the mass density of each cluster component with the total mass density in the left panel of Fig. 8. Their relative fraction with respect to the total mass is shown in the right panel of Fig. 8. We add a fit by a generalised Navarro-Frenck-White profile (gNFW; Zhao 1996) of the total mass density as a qualitative comparison to the model mass slope. In contrast to the projected profile presented in Fig. 7, there is a clear domination of the baryonic mass of the BCG up to around 20 kpc which is approximately the BCG half-light radius (i.e. 17 kpc). The ICM becomes the main baryonic contributor at radii larger than the projected counterparts, i.e. around 50 kpc. Considering the total mass, the gNFW profile can provide a good fit to the total mass from 20 kpc and up to the end of the constrained area. Hence, it is unable to account for the BCG mass distribution when it dominates in the inner core, which can be put in perspective of the results obtained by Newman et al. (2013) where a dPIE was added to account for the BCG in addition to the gNFW profile. In our case, we obtain a slope  $\beta = 0.20^{+0.02}_{-0.03}$ , significantly lower than 1, where 1 is the slope of a NFW profile. Similarly, Cerny et al. (2025) presented a sample of cluster mass models where the BCG kinematics was used along strong lensing to constrain the model parameters. In contrast

to this work, in their models the mass component are all modelled with dPIEs and they rely on a scaling for the cluster member based on the Faber & Jackson law (Faber & Jackson 1976). We reproduce their slope measurement  $\gamma = -\frac{d \log_{10}(\rho)}{d \log_{10}(r)}$  over 5 to 50 kpc for the DM distribution ( $\gamma = 0.173^{+0.007}_{-0.007}$ ) and the total mass with the BCG & ICL subtracted ( $\gamma = 0.175^{+0.006}_{-0.006}$ ). Contrary to their results, we obtain the same measurement for the total mass without the BCG as both profile present a cored distribution. A possible source for that difference is the cluster member modelling, as once the BCG has been subtracted, their models reduce to the DM and cluster member mass components.

Our results highlight the importance of providing an accurate census of the baryonic components to robustly recover the DM profile down to the few kpc of the inner core. In particular, the DM profile's shape in that area is sensitive to alternatives to the cold DM (CDM) paradigm, such as self-interacting or Fuzzy DM models that present a cored distribution instead of the cuspy CDM profile. Parameters of these DM models are correlated to the shape and size of these cores, making our modelling well-suited to measure them robustly (Robertson et al. 2021).

Another advantage of our self-consistent approach, which relies on disentangling each cluster components, is its ability to assess which baryonic component is the best tracer of DM. It is particularly useful in the context of clusters or groups that do not present lensing features,

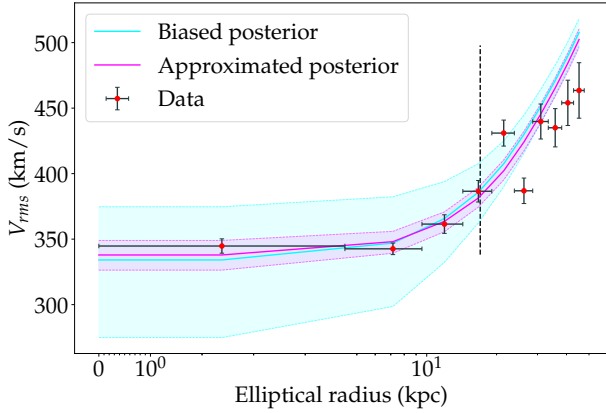


**Figure 5.** Stellar kinematic data and model of the BCG & ICL component as a function of the elliptical radius in kpc. The cyan distribution represents the biased posterior before the importance sampling step, while the magenta one is the approximated posterior after the resampling procedure. The scattered points represent the observational data points. The elliptical radius is defined with the same ellipticity as used for the fit of the  $V_{\text{rms}}$ . The shaded area represents the  $3\sigma$  uncertainties of each posterior, while the plain lines highlight the median. The errors of the data points represent the standard deviation of the  $V_{\text{rms}}$  fit. The dashed black vertical lines show the BCG half-light radius as measured by Tortorelli et al. (2018) of 17 kpc

but deep observations can map some of their baryonic components and then recover an estimated DM profile. For example, the previous analysis by Montes & Trujillo (2019) presented evidence for the ICL to be a good tracer of the DM profile slope.

However, we leave analyses such as measuring DM properties or assessing which baryonic components are the best DM tracers to future work. Before concluding, we must address the reliability of our stellar mass estimates, as inaccurate BCG & ICL stellar content could introduce significant bias into the analysis presented above.

## 5 DISCUSSION

We choose to focus the discussion on the estimate of the new baryonic components added to the self-consistent multi-probe approach developed in B24. We start in Sect. 5.1 by analysing our estimate of the BCG & ICL stellar mass in light of the SED estimates provided in B25a (section 5.3). We follow up in Sect. 5.2 and 5.3, where we discuss the probable biases of BCG & ICL stellar mass estimates with the neglected BCG super massive black hole (SMBH) and assumption of the BCG & ICL stellar kinematics. We then discuss our estimate of the SsHMR and its dependence on the initial stellar mass estimated from cluster members in Sect. 5.4 and 5.5.

### 5.1 BCG & ICL stellar masses estimate

Fig. 9 presents the estimates of the stellar-mass-to-light ratio of the BCG & ICL component. It compares the estimates from each mass model with a “BCG - ML 2” parametrisation with the SED fit results provided in B25a (section 5.3). For each mass model, there is an apparent discrepancy between the estimate from LENSTOOL and the SED fit within the BCG (i.e.  $R_e = 17$  kpc). In contrast, at larger radii, both estimates agree within their  $1\sigma$  CI for the LePHARE SED model. The models with a double power-law and a delayed SFH present a less

good agreement with the SED estimate, although  $\Upsilon_{*,\text{SED}}^{\text{BCG}}$  is included in the  $3\sigma$  CI of  $\Upsilon_{*,\text{lt}}^{\text{BCG}}$ . These results are in line with the stellar-mass-to-light ratio mismatch observed in early-type galaxies (ETG) between SED and stellar kinematics estimate (see Smith (2020) for a review). These mismatches are observed when the kinematic analysis relies on a constant value for the BCG,  $\Upsilon_*$  Posacki et al. (2015); Lu et al. (2024). We are in a similar case as our varying  $\Upsilon_{*,\text{lt}}^{\text{BCG}}$  parametrisation has only one coefficient associated with the BCG. Oldham & Auger (2018) and Collett et al. (2018) find evidence for a steep gradient of  $\Upsilon_*$  within ETGs associated with an IMF variation with radius from a Salpeter (1955) IMF to a Milky-way like IMF that would produce such a mismatch. As reported by Mehrgan et al. (2024), such gradients are visible for very small radii,  $R \lesssim 1$  kpc, which cannot be probed with our datasets. In addition to this picture, our results suggest that the ICL in AS1063 follows a Milky-way like IMF. Hence, the BCG and the ICL would present a similar IMF at their common border.

These discrepancies in the estimate of the stellar-mass-to-light ratio imply a larger stellar mass for the BCG & ICL component than estimated in B25a (section 5.3). We obtain  $1.59 \pm 0.24$ ,  $1.52 \pm 0.21$  and  $1.30 \pm 0.29 \times 10^{12} M_\odot$  for the model with a delayed SFH, double power-law SFH and LePHARE SED models, respectively. These masses are estimated within the same elliptical bins as presented in B25a (section 5.2). These new estimates are from 48 to 133 per cent higher than their SED counterparts, which are mostly due to the underestimation of the BCG stellar mass. The model with a delayed SFH and double power-law SFH, which presents discrepancies larger than 100 per cent, also includes a higher estimate of the stellar mass within the ICL.

To further compare our results and in particular the  $\Upsilon_*$  estimate mismatches, we define the following mismatch parameter  $\alpha$ :

$$\alpha = \frac{\Upsilon_{*,\text{lt}}^{\text{BCG}}}{\Upsilon_{*,\text{SED}}^{\text{BCG}}} \quad (24)$$

We estimate the posterior distribution of  $\alpha$  by propagating the distribution of  $\Upsilon_{*,\text{lt}}^{\text{BCG}}$  from mass models with a single evaluation of  $\Upsilon_{*,\text{SED}}^{\text{BCG}}$  represented by its median. We do not include the uncertainty of  $\Upsilon_{*,\text{SED}}^{\text{BCG}}$  as it is negligible for two SED models, and we do not have the full posterior shape for every SED fit, in particular the one made with LePHARE. We compare  $\alpha$  with the results from Lu et al. (2024), who analysed the IMF variation for the MaNGA DynPop project. This project aimed at observing 10000 early type galaxies (ETGs) to perform dynamical and stellar population synthesis analyses. In particular, they estimate  $\alpha$  as a function of the galaxy velocity dispersion,  $\sigma_e$ , for a Salpeter (1955) IMF. We convert their results to a Milky-way like IMF following the conversion factor provided in Wright et al. (2017), and we use a value of 341 km/s for  $\sigma_e$ , which has been measured in the most central bins of our BCG & ICL stellar kinematics measurement.

The top row of Fig. 10 presents the estimation of  $\alpha$  compared to the results of Lu et al. (2024). The  $3\sigma$  CI of each model agrees with the expected mismatch from Lu et al. (2024) for the data points within the BCG. However, the agreement gets weaker towards the cluster centre. Indeed, the  $1\sigma$  CI of only the two/three last data points of the BCG agree with the expected mismatch. It may indicate an overestimate of  $\Upsilon_{*,\text{lt}}^{\text{BCG}}$  at the first data point if the BCG is not an outlier of the Lu et al. (2024) relations. This could be due to the presence of a SMBH with a mass above the  $M_\bullet - \sigma_e$  relation as we discuss in Sect. 5.2. The assumption behind the BCG & ICL stellar kinematic models may also have an influence. A JAM model assumes a single ellipticity and a Gaussian line-of-sight velocity distribution. A lower ellipticity would

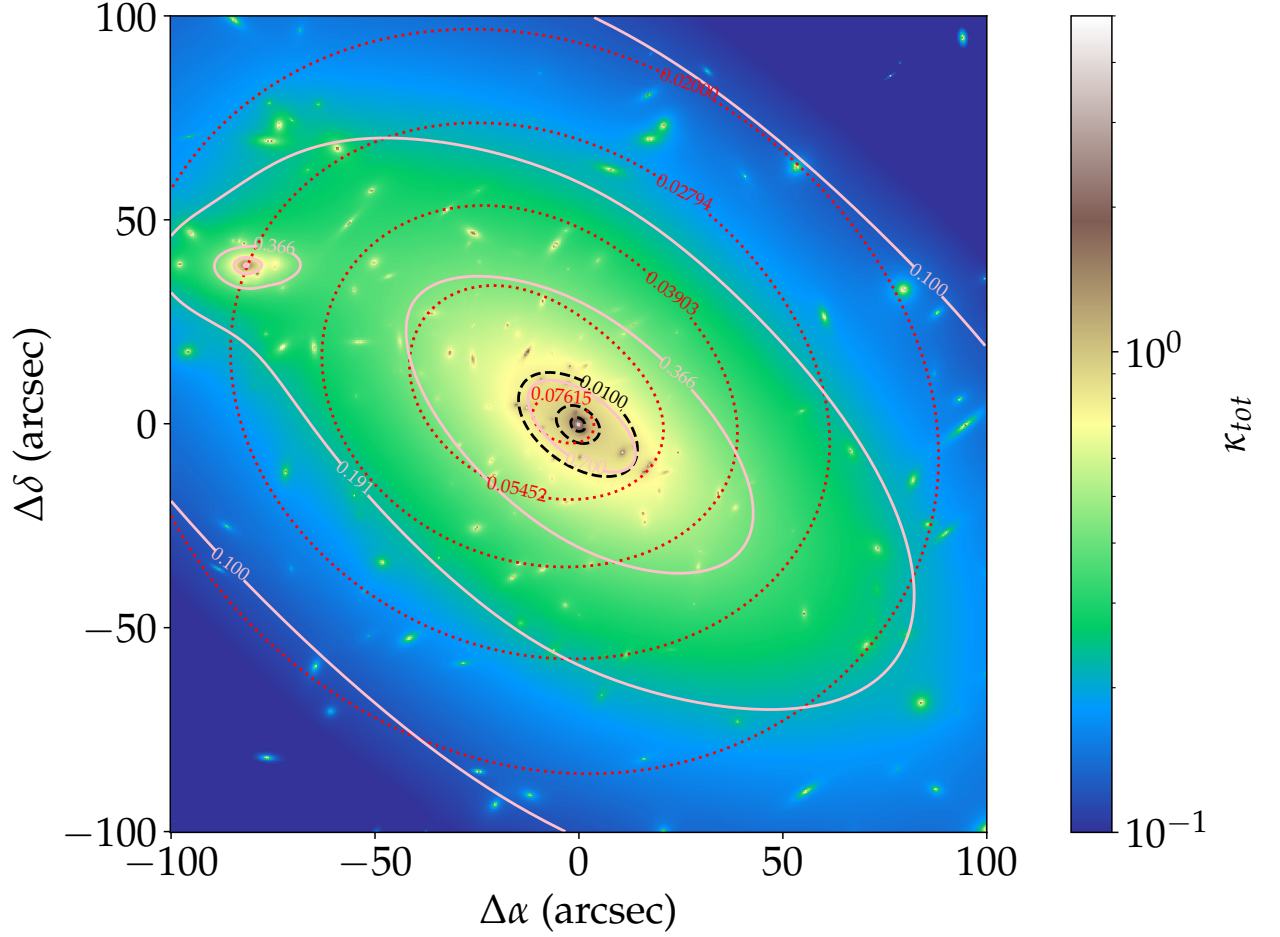


**Figure 6.** 2D normalised surface mass density (convergence) associated with the total mass distribution. Each cluster-scale mass component is highlighted by contours. The BCG & ICL baryons are highlighted in dashed black, while the intra-cluster gas and DM are in dotted red and solid pink contours, respectively.

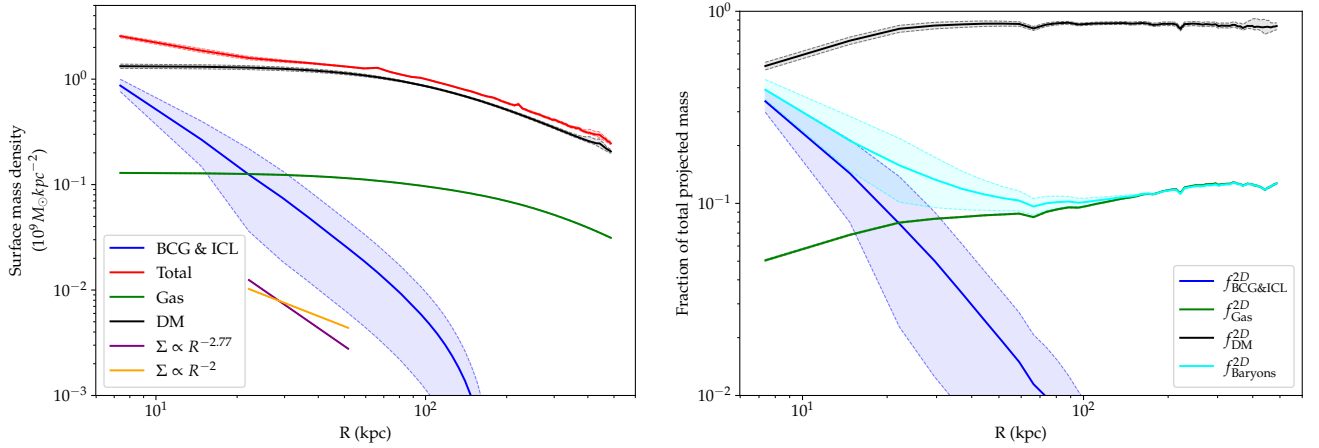


**Figure 7.** *Left panel:* Surface mass density of the whole cluster (red) and each of its components: the cluster-scale DM component (black), the BCG & ICL baryons (blue) and the gas (green). The plain lines represent the median of each distribution among the model posterior while the shaded area shows its  $3\sigma$  CI. As a qualitative comparison to BCG & ICL profile slope, we present two power-law profiles with a slope of  $-2$  and  $-2.77$  (best fitting solution on the BCG & ICL profile), respectively. *Right panel:* Projected fraction of each cluster mass component relative to the total mass. It shows the same profile as in the left panel but is divided by the median of the total mass density profile. In addition, we also provide the profile of the cluster-scale component baryons, combining the gas and BCG & ICL components. The colour scheme and meaning of the plain line and shaded area are the same as in the left panel. The combined baryonic profile is presented in cyan.

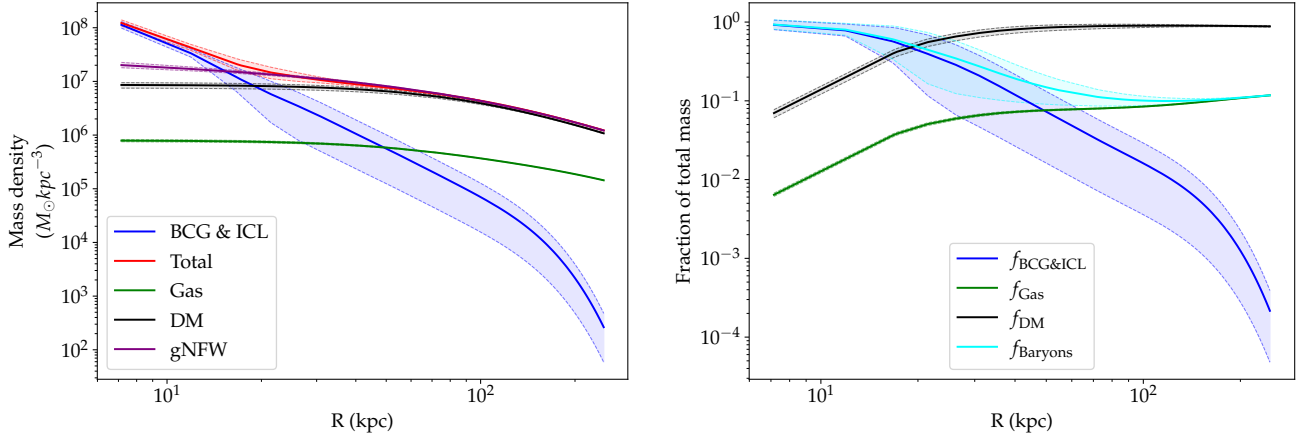


**Figure 8.** *Left panel:* Mass density of the whole cluster (red) and each of its components: the cluster-scale DM component (black), the BCG & ICL baryons (blue) and the gas (green). A gNFW fit to the total mass distribution is presented as a comparison to model the mass slope. Plain lines represent the median of each distribution among the model posterior, while the shaded area shows its  $3\sigma$  CI. *Right panel:* Fraction of each cluster mass component relative to the total mass. The profile of the cluster-scale component baryons is simply the sum of the gas and BCG & ICL components. The colour scheme and meaning of the plain line and shaded area are the same as in the left panel. The combined baryonic profile is presented in cyan.

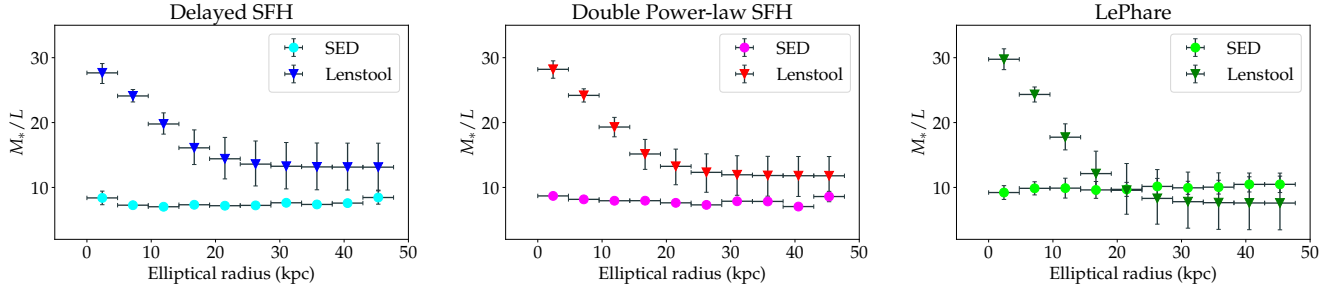


**Figure 9.** Stellar-mass-to-light ratio of the BCG & ICL component,  $Y_{*,\text{lt}}^{\text{BCG}}$  for the three models with a “BCG - ML 2” parametrisation with their equivalent estimated through SED fitting,  $Y_{*,\text{SED}}^{\text{BCG}}$  as a function of the elliptical radii defined in B25a (section 5.2). Error bars represent the  $1\sigma$  CI for both  $Y_{*,\text{SED}}^{\text{BCG}}$  estimates, while errors on the radius represent the width of the elliptical bins in which it is averaged. Each model uses a different SED model. They are presented in the following order from *left to right*: Delayed SFH, double power-law SFH and LePhare. The colour schemes highlight  $Y_{*,\text{lt}}^{\text{BCG}}$  (blue, red and green) with darker colours than  $Y_{*,\text{SED}}^{\text{BCG}}$  (cyan, magenta and lime). Similar colours regroup models that are associated with the same SED model.

increase the  $V_{\text{rms}}$  of the kinematic model at a fixed mass, which may reduce the  $Y_{*,\text{lt}}^{\text{BCG}}$  required at the first data point. However, a scheme with varying ellipticity should be employed to avoid an increase of  $V_{\text{rms}}$  within the ICL. Similarly, a misalignment with the light tracer and mass distribution that is forbidden by the axisymmetric requirement of the JAM method would result in deviation from a Gaussian distribution for the line-of-sight velocity distribution. A proper assessment of such bias requires a 3D modelling method such as Schwarzschild’s orbit-superposition (Bovy 2015), but it is out of the scope of this work. In Sect. 5.3, we try to correct the effect of possible deviation from a Gaussian line-of-sight velocity distribution by refitting these velocity distributions without the extra-moments,  $h_3$  and  $h_4$ .

## 5.2 BCG SMBH

In our modelling, we neglect the influence of a SMBH which mass can be degenerated with the BCG stellar mass. Hence, to assess the reliability of  $Y_{*,\text{lt}}^{\text{BCG}}$  estimates to that bias, we add a point mass profile with a fixed position at the BCG centre in the lensing mass model.

We modify our stellar kinematic model by adding a SMBH with its mass contained in the point mass profile of the lensing model. We apply these modelling changes to each “BCG - ML 2” model and reproduce the whole optimisation procedure presented in Sect. 3.

We apply this procedure for two SMBH priors, one assuming the mass from the  $M_\bullet - \sigma_e$  relation compiled in van den Bosch (2016) and another wider prior to test the deviation from this relation. Using the relation of van den Bosch (2016), we obtain  $M_\bullet = 3.66^{+0.62}_{-0.53} \times 10^9 M_\odot$  using the uncertainties from their relation fit and our best-fitting velocity dispersion in the first bin (i.e.  $\sigma_{\text{BCG}} = 341 \text{ km/s}$ ). The associated prior is a Gaussian distribution with the  $M_\bullet$  median as the mean and half of the distance between the two quantiles as a standard deviation. For the wider prior, we intentionally use a particularly wide log uniform prior from  $10^7$  to  $10^{11} M_\odot$ .

When the SMBH is assumed from the  $M_\bullet - \sigma_e$  relation, we observe mostly negligible changes to the model parameters and the reproduction of the constraints, except for the model with a double power-law SFH, which provides a better fit to the stellar kinematics. Besides that model, which exhibits a significant reduction of the WAIC from  $-33553$  to  $-33534$ , it remains unchanged for the two other SED

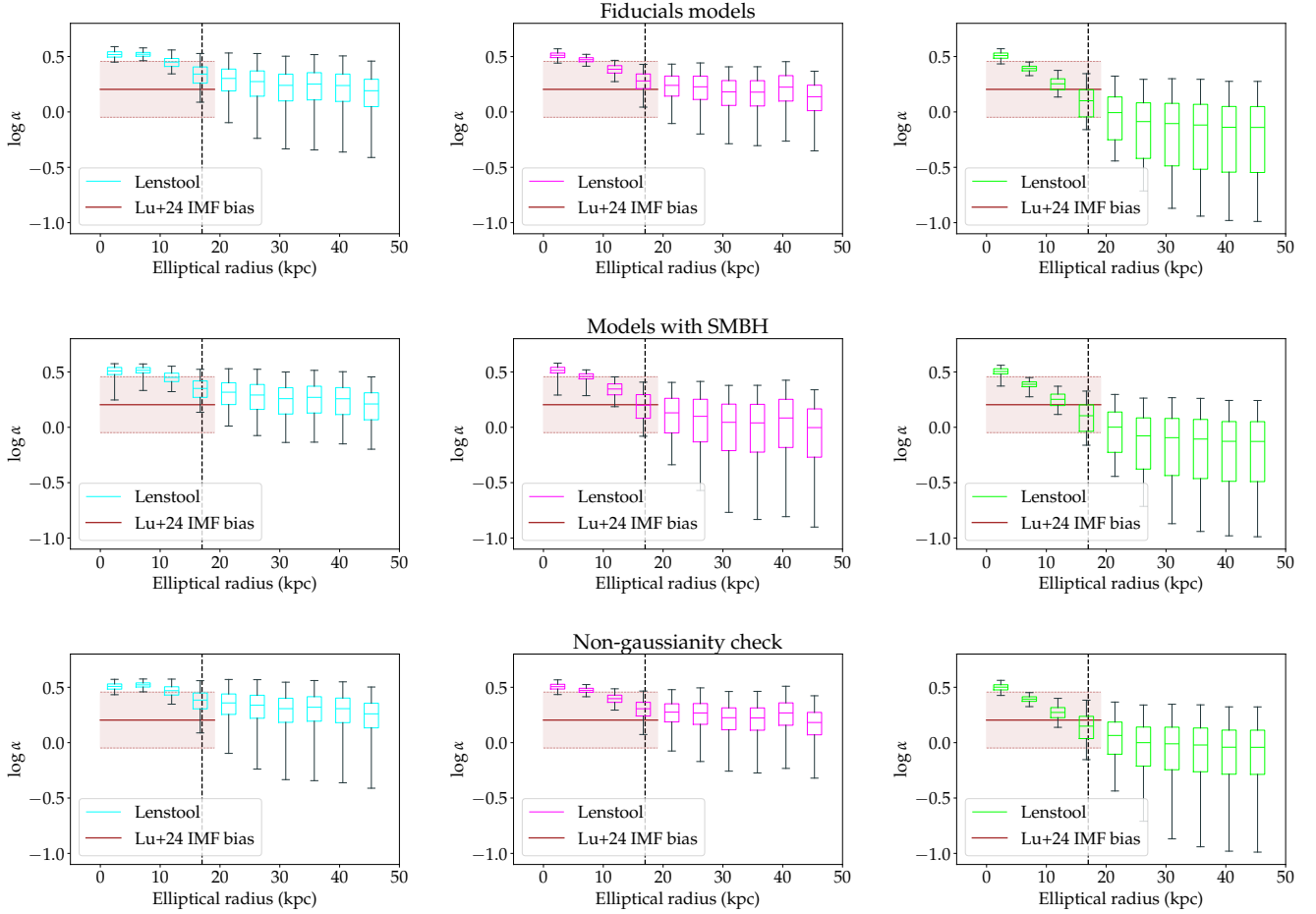


**Figure 10.** Stellar-mass-to-light ratio mismatch parameter  $\alpha$  as a function of the elliptical radius defined in B25a (section 5.2). In each plot, we highlight the BCG size using its half-light radius, represented by the dashed black line. The shaded brown area represents the expected mismatch due to IMF variation in early-type galaxies as reported by Lu et al. (2024). The width of this area represents 3 times the standard deviations from Lu et al. (2024) fit, while the plain line represents their best-fitting solution. The  $1\sigma$  CI and  $3\sigma$  CI of the posterior distribution of  $\alpha$  are represented by the boxes and the associated error bars, respectively. The median is highlighted by the horizontal bars within each box. Each column represents a model with a “BCG - ML 2” parametrisation that used different SED models for the cluster member components. They are ordered from *left to right*: BAGPIPES Delayed SFH, BAGPIPES double power-law SFH and LEPHARE. The colour scheme of the boxes represents the associated SED models. Each row represents a different test. *Top row*: Mass models with the methodology outlined in this work. *Middle row*: Mass models with a central SMBH. *Bottom row*: Mass models where the kinematic models of the BCG & ICL component are compared against the observed kinematics, in which we account for the deviation from Gaussian stellar velocity distributions.

parametrisations. The posterior on  $\Upsilon_{*,\text{lt}}^{\text{BCG}}$  is mostly the same with a slight decrease of the  $1\sigma$  CI width within the ICL. It shows that neglecting the BCG SMBH, which would follow the  $M_\bullet - \sigma_e$  relation, does not significantly affect the estimate of  $\Upsilon_{*,\text{lt}}^{\text{BCG}}$ .

With the larger prior on the SMBH mass, we obtain a better reproduction of the stellar kinematics only with the model with a double power-law SFH, similarly to the previous case. However, there are larger changes in the model parameter, and in particular with  $\Upsilon_{*,\text{lt}}^{\text{BCG}}$ . These changes appear in the width of the  $3\sigma$  CI while the median and  $1\sigma$  CI tend to stay the same as the model without SMBH. As our constraints on the SMBH are weak, the modification of  $\Upsilon_{*,\text{lt}}^{\text{BCG}}$  can be overestimated. The constraints are too weak to allow for setting a higher bound on the SMBH mass for all three models. The middle row of Fig. 10 presents the mismatch parameter,  $\alpha$ , for these three models. The data points within the BCG highlight the modification of the  $3\sigma$  CI, which overlap more favourably with the expected mismatch from Lu et al. (2024). It indicates that a SMBH with masses above the  $M_\bullet - \sigma_e$  relation can lead to an overestimation of  $\Upsilon_{*,\text{lt}}^{\text{BCG}}$ .

within the BCG. However, our dataset is not sufficient to assess the presence of such SMBH.

Another aspect of the SMBH addition is the slight modification of  $\Upsilon_{*,\text{lt}}^{\text{BCG}}$  within the ICL, as the  $3\sigma$  CI of the double power-law SFH and LEPHARE SED models are closer to each other than previously. In the case of the double power-law SFH,  $\Upsilon_{*,\text{lt}}^{\text{BCG}}$  are in better agreement with  $\Upsilon_{*,\text{SED}}^{\text{BCG}}$  than before, as the  $1\sigma$  CI is now including  $\log \alpha = 0$ . In contrast, the model with a delayed SFH, presents a narrower  $3\sigma$  CI which barely includes the horizontal line at  $\log \alpha = 0$ . Hence, it points toward a more complex correlation with other model components rather than a degeneracy of the mass between the BCG & ICL and SMBH.

### 5.3 Non-gaussianity of the BCG stellar velocity distribution

In B25a (section 5.2), we fit the line-of-sight velocity distribution assuming a Gaussian modified by a Gauss-Hermite expansion. In our parametrisation, only the coefficients for the third and fourth Hermite

polynomials are non-zero (i.e. parameters  $h_3$  and  $h_4$ ). To account for the  $V_{\text{rms}}$  differences if the velocity distribution is purely Gaussian, we fit a Gaussian distribution to the velocity distribution obtained in B25a. It mostly affects points in the ICL, as they present larger values for  $h_4$  of around 0.05. Hence, we observe an opposite pattern from Gavazzi (2005), as the deviation from Gaussianity appears at a larger radius than closer to the cluster centre.

We reproduce the importance sampling procedure with those modified  $V_{\text{rms}}$ , and the impact on the mismatch parameter is presented in the bottom row of Fig. 10. It does not change the agreement with the (Lu et al. 2024) expected mismatch for the BCG, although models tend to prefer slightly higher  $\Upsilon_{*,\text{lt}}^{\text{BCG}}$  for the ICL. In particular, the model with LEPHARE has a narrower  $1\sigma$  CI as its lower tails lean towards higher  $\Upsilon_{*,\text{lt}}^{\text{BCG}}$ . Hence, the deviation from a Gaussian stellar velocity distribution does not impact  $\Upsilon_{*,\text{lt}}^{\text{BCG}}$  in the BCG according to this test. However, it leaves other deviations from the JAM method, such as varying ellipticity as possible biases that we leave for future work.

These two tests regarding our estimate of  $\Upsilon_{*,\text{lt}}^{\text{BCG}}$  highlight the robustness of our modelling as they did not have much influence on the final results. We note that the SMBH could have a significant impact, although the required SMBH mass would be quite large, and such an object would be an outlier of the SMBH populations. It is promising as this comprehensive modelling will allow for DM constraint based on the DM-only profile free of any baryonic mass, such as self-interacting cross-section, which can be estimated based on the baryonic and DM mass distribution (Robertson et al. 2021).

#### 5.4 stellar-to-subhalo mass relation

Thanks to our new modelling of cluster members, we can estimate the stellar-to-subhalo mass relations (SsHMR) with the double power-law defined in Sect. 2.2 for the most central galaxies in clusters. Such relations are measured in cosmological simulations, and they should vary during the infall of galaxies within their host cluster (Niemiec et al. 2019): the increase of stellar mass stops as galaxies are quenched by the cluster environment, while the outside-in stripping of DM by tidal forces of the cluster decreases sub-halo masses. In addition, self-interacting DM could cause an additional ‘evaporation’, thus further decreasing sub-halo masses during their infall (Bhattacharyya et al. 2022; Sirks et al. 2022). As galaxies that have spent a longer time in their host cluster tend to be located closer to the core, precisely measuring the radial evolution of the SsHMR could allow us to quantify the impact of tidal stripping, as well as possible evaporation due to DM self-interactions. Stacked galaxy-galaxy weak lensing analyses have put some constraints on the SsHMR (Li et al. 2016; Sifón et al. 2015; Niemiec et al. 2017; Sifón et al. 2018; Wang et al. 2024), but these measurements do not reach the cluster core, where the effects of stripping should be the highest. To make the fairest comparisons, the types of galaxies (i.e. early or late type galaxies) and their distances to the cluster core should be considered (Niemiec et al. 2022). In particular, Niemiec et al. (2022) reported a double power-law fit of the SsHMR for central galaxies in the IllustrisTNG (Pillepich et al. 2018; Weinberger et al. 2017) simulation. They reported the fit of the whole sample of central galaxies but also for different subsets depending on the galaxy type, redshift bin or the galaxy distance to the cluster core. Hence, to match the sample of galaxies considered from IllustrisTNG to our observational measurements, we combine different SsHMR to match the properties of our sample. We sample 1000 SsHMRs, where 19 per cent of the sample follows the SsHMR for central late-type galaxies. This proportion matches the proportion

of late-type galaxies in our cluster member sample as found by visual inspection. We classify cluster members as late-type galaxies if they exhibit complex morphologies with possible spiral arms or colour difference from the bulk of the population. We model the rest of the sample, assuming the SsHMR from central early-type galaxies with a radius inferior to the maximal distance from the cluster core of a modelled cluster member. Hence, the radial dependencies of the SsHMR are only included for early-type galaxies, as this dependence has not been probed by Niemiec et al. (2022) for late-type galaxies.

The left panel of Fig. 11 presents the comparison of the SsHMR from IllustrisTNG with our measurement for each model with a ‘BCG - ML 2’ parametrisation. The  $1\sigma$  CI of the SsHMR of our three models and IllustrisTNG overlap over the entire stellar mass range, from  $10^{8.5}$  to  $10^{11.5} M_{\odot}$ . We notice that our results are systematically above the median SsHMR measured from the simulation. It may highlight some discrepancies between our model and the simulation SsHMR on subsamples, such as selections based on the galaxy types, i.e. only early or late-type galaxies. As in the current modelling, we do not distinguish between the two types of galaxies; we leave any further analyses to future work.

Each SED model used to estimate the cluster member  $M_*$  leads to slightly different SsHMRs, which agree at most for  $M_* \approx 10^{10} M_{\odot}$  with an increasing divergence as  $M_*$  increases or decreases. Hence, we observe the double power-law SFH model that provides higher  $M_*$  for the most massive cluster members, and lower  $M_*$  for the least massive. The model with LEPHARE SED presents an opposite pattern, while the model with a delayed SFH is close to the double power-law one to a lesser extent. Even if their  $1\sigma$  CI overlap with IllustrisTNG, they present different slopes. It may indicate some discrepancies in the details of the different galaxy populations within AS1063. Increasing the mass range of  $M_*$  above  $10^{11.5} M_{\odot}$  would likely lead to a disagreement between our results and simulation, particularly when considering the double power-law SFH model.

#### 5.5 Cluster member IMF variation

In our SsHMR estimate, we use a fixed estimation of the cluster member  $M_*$  as the posterior median from the SED fit. These SED models assume a Milky-Way like IMF, which does not agree with the kinematic modelling of early-type galaxies (Posacki et al. 2015; Lu et al. 2024). We use the best-fitting relation from Lu et al. (2024) for the expected mismatch between SED and kinematic estimate of  $M_*$  to correct our SED estimate of  $M_*$ . We estimate  $\sigma_e$  for each cluster member based on their mass and light distribution as we do for the cluster member likelihood (see Sect. 3.3) and assume the best-fitting mass model. We apply this correcting factor to each cluster member in our sample without distinguishing between early- and late-type galaxies.

The right panel of Fig. 11 presents the SsHMR with the correcting factor applied to  $M_*$  estimates with the SsHMR from IllustrisTNG. Similarly to the uncorrected SsHMR, the  $1\sigma$  CI of the observation and simulation overlap. We also observe that the SsHMR followed in AS1063 is systematically higher than the median SsHMR from the IllustrisTNG. Although at the massive end, there is a better agreement with the trend between observations and simulations, as there is no tendency for discrepancies at  $M_* \approx 10^{10.75} M_{\odot}$  or above.

We try to optimise new mass models with the correct  $M_*$ , although the obtained best-fit model  $\sigma_e$  are not in agreement with the one used to estimate the correcting factor for  $M_*$ . These differences in correcting factors are above 50 per cent for some cluster members. Hence, we reject these models. The correcting formula from Lu et al. (2024) as a polynomial of degree 1 could be added to our modelling

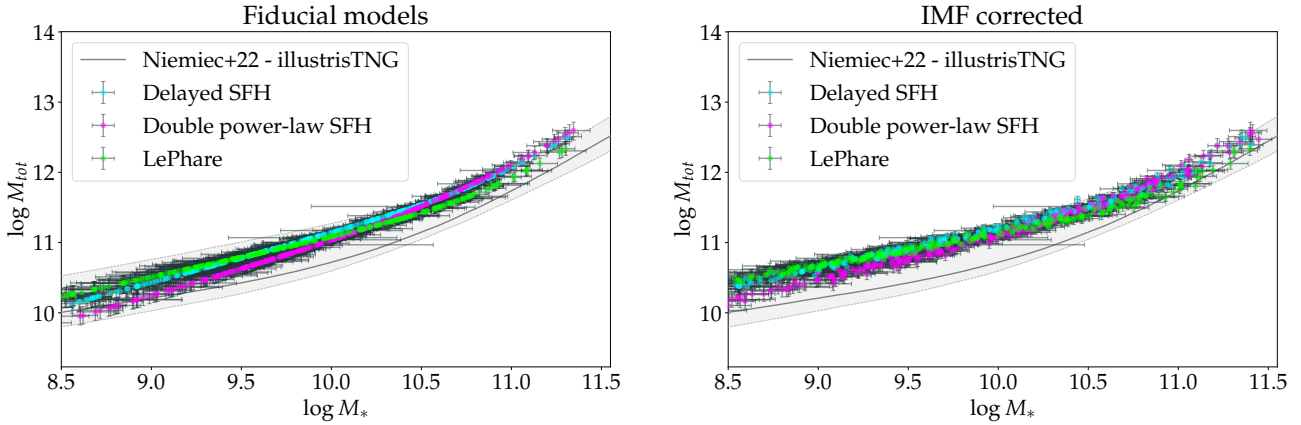


**Figure 11.** Stellar-to-subhalo mass relation measured in this work compared to the results from the illustrisTNG simulations as reported in Niemiec et al. (2022). We represent our estimate through each cluster member. The position of the colour points represents the median of their stellar masses as given by the SED fitting or the total mass from the model posterior distribution. The error bars show the  $1\sigma$  CI for those distributions. Each colour represents different SED models with the Delayed SFH, double power-law SFH and LePhare models shown in cyan, magenta and lime, respectively. The results from the IllustrisTNG simulation are represented by the grey area, which shows the  $1\sigma$  CI, while the plain lines show the median. The *left panel* presents stellar-to-subhalo mass relations as defined in the mass models, while the *right panel* presents the same relation with the stellar masses being corrected for the IMF variation as reported in Lu et al. (2024). The IMF correction is based on the model-predicted velocity dispersion,  $\sigma_e$ , for the best-fitting model.

of cluster members with a split between early and late-type galaxies. It could be a new way of estimating IMF variations within the cluster galaxy population.

Our new modelling of cluster members appears to be a robust method to estimate the SsHMR, as the general trend agrees with large-scale simulation results. The estimate of cluster member total masses seems consistent between each SED model, as the slope difference between them is expected from the difference in stellar masses. As highlighted by the slight differences between our results and illustrisTNG, anomalies may be found between observations and simulations, which can highlight differences in how the cluster environment strips DM in real cases.

## 6 CONCLUSION

In this series of two papers, we present the first mass modelling method that allows us to fully disentangle DM at the galaxy- and cluster-scale, but also each baryonic component. To achieve such details, we rely on multiple mass probes to specifically constrain the baryonic components with X-ray surface brightness or multi-band photometry. We combine total mass constraints from the BCG & ICL stellar kinematics and strong lensing to constrain the mass profile from  $\approx 5$  to 250 kpc, and use cluster member velocity dispersions to measure their total masses. We detail how we gather these sets of constraints in B25a.

Here, we focus on the mass modelling methodology and results. We test different parameterisations for the BCG & ICL components, which favour a varying  $Y_*^{\text{BCG}}$  with radius. In our case, a simple model with two coefficients, one for the BCG and one for the ICL, is favoured. In addition to providing a comprehensive mass model of AS1063, with each cluster component disentangled, we reduce the uncertainties on the total mass profile by 20–30 per cent, depending on the considered radii. It allows us to measure the DM only profile with an error of less than 5 per cent over the entire considered region. We obtain these results while presenting one of the most complex parametric mass models.

We then discuss the robustness of the estimates of the stellar masses

contained in the BCG & ICL component, as well as cluster members. We found that the stellar mass of the ICL agrees at  $3\sigma$  with a Milky-Way like IMF as fitted through three different SED models. We find that the BCG requires a larger  $Y_*^{\text{BCG}}$  that can be explained by the IMF variation observed in early-type galaxies, although AS1063 BCG is in the tails of the early-type galaxies distribution modelled by Lu et al. (2024). We look for over- or under-estimates of  $Y_*^{\text{BCG}}$  by adding a SMBH in the BCG and accounting for deviations from a Gaussian velocity distribution. Besides a SMBH with a mass above the  $M_\bullet - \sigma_e$  relation, we find no significant influence on  $Y_*^{\text{BCG}}$ .

Regarding cluster members, we analyse our estimates of their total and stellar masses by comparing the SsHMR included in the model with results from the large-scale simulation IllustrisTNG (Niemiec et al. 2022). We find a  $1\sigma$  CI agreement between the observational and simulated relations, although with some discrepancy at the higher mass end ( $> 10^{10.75} M_\odot$ ) for the delayed and double power-law SFH models. When accounting for the IMF variations with the Lu et al. (2024) correction formula, we find a slightly better agreement for the massive end, as no data points are outside the  $1\sigma$  CI of the IllustrisTNG result. More detailed comparisons in future works will enable us to refine the comparison and potentially identify discrepancies between observations and simulations for subsets of the galaxy populations.

In this series, we extend the framework from B24 to obtain a complete picture of the cluster mass distribution. This method can be further improved via a better treatment of the constraints or modelling hypotheses. With the development of hardware accelerators, the next logical step appears to be considering the full light information provided by multiple images, similar to what is done routinely with galaxy-scale lenses (e.g. Nightingale et al. 2021). At cluster-scale, it is already possible to reconstruct a multiple image system at fixed mass model (e.g. Sharma et al. 2021), although the combination of both the reconstruction and mass model optimisation has been out of reach. Acebron et al. (2024) is paving the way in that direction as they used a hybrid approach, where they combined the reconstruction of a single lensing system with the usual point-like approximation for the other systems.

Beyond the methodological considerations, applying our method to a sample of clusters, ideally relaxed, will be instrumental in constraining DM properties by allowing for the precise estimation of the DM only profile. Crucially, our approach is the first step to reproduce the treatment of Robertson et al. (2021) on observations to measure the self-interacting DM cross-sections, as we have an accurate census of the baryonic distribution. This method can also be leveraged to develop similar analyses for alternative DM models (e.g. fuzzy DM profile from Chan et al. 2022) but also modified gravity, allowing us to set constraints beyond the single scope of the self-interacting DM paradigm.

The broader application of this method depends on the availability of comprehensive multi-wavelength datasets, which currently exist for only a limited number of clusters, such as the Hubble Frontier Fields. This work advances cluster mass modelling to new methodological and observational frontiers, establishing the observational framework required for the precise characterisation of the DM distribution.

## ACKNOWLEDGEMENTS

The authors thank Massimo Meneghetti, Raphaël Gavazzi, Michaela Hirschmann, and Mireia Montes for their helpful discussions at various stages of the project. The computations were performed at the University of Geneva using Yggdrasil and Boabab HPC services. BB acknowledges the Swiss National Science Foundation (SNSF) for supporting this work. ML acknowledges the Centre National de la Recherche Scientifique (CNRS) and the Centre National des Etudes Spatiales (CNES) for support. MJ is supported by the United Kingdom Research and Innovation (UKRI) Future Leaders Fellowship ‘Using Cosmic Beasts to uncover the Nature of Dark Matter’ (grant number MR/X006069/1).

## DATA AVAILABILITY

Mass models with a “BCG - ML 2” are available at the following repository.

## REFERENCES

- Acebron A., et al., 2024, arXiv e-prints, p. [arXiv:2410.01883](https://arxiv.org/abs/2410.01883)
- Akaike H., 1998, *Information Theory and an Extension of the Maximum Likelihood Principle*. Springer New York, New York, NY, pp 199–213, doi:10.1007/978-1-4612-1694-0\_15, [https://doi.org/10.1007/978-1-4612-1694-0\\_15](https://doi.org/10.1007/978-1-4612-1694-0_15)
- Balestra I., et al., 2013, *A&A*, **559**, L9
- Beauchesne B., 2025, A comprehensive separation of dark matter and baryonic mass components in galaxy clusters I: Mass constraints from Abell S1063
- Beauchesne B., Clément B., Richard J., Kneib J.-P., 2021, *MNRAS*, **506**, 2002
- Beauchesne B., et al., 2024, *MNRAS*, **527**, 3246
- Bergamini P., et al., 2019, *A&A*, **631**, A130
- Bhattacharyya J., Adhikari S., Banerjee A., More S., Kumar A., Nadler E. O., Chatterjee S., 2022, *ApJ*, **932**, 30
- Bonyadi M. R., Michalewicz Z., 2017, *Evolutionary Computation*, **25**, 1
- Bovy J., 2015, *ApJS*, **216**, 29
- Buchner J., 2019, *PASP*, **131**, 108005
- Buchner J., 2021, *The Journal of Open Source Software*, **6**, 3001
- Buchner J., et al., 2014, *A&A*, **564**, A125
- Cappellari M., 2008, *MNRAS*, **390**, 71
- Cappellari M., 2020, *MNRAS*, **494**, 4819

- Cerny C., Jauzac M., Lagattuta D., Niemiec A., Mahler G., Edge A., Massey R., 2025, *arXiv e-prints*, p. [arXiv:2506.21531](https://arxiv.org/abs/2506.21531)
- Chan H. Y. J., Ferreira E. G. M., May S., Hayashi K., Chiba M., 2022, *MNRAS*, **511**, 943
- Collett T. E., et al., 2018, *Science*, **360**, 1342
- Dutton A. A., et al., 2011, *MNRAS*, **417**, 1621
- Elíasdóttir Á., et al., 2007, *arXiv e-prints*, p. [arXiv:0710.5636](https://arxiv.org/abs/0710.5636)
- Faber S. M., Jackson R. E., 1976, *ApJ*, **204**, 668
- Gavazzi R., 2005, *A&A*, **443**, 793
- Granata G., et al., 2022, *A&A*, **659**, A24
- Hol J. D., Schon T. B., Gustafsson F. K., 2006, 2006 IEEE Nonlinear Statistical Signal Processing Workshop, pp 79–82
- Jullo E., Kneib J. P., Limousin M., Elíasdóttir Á., Marshall P. J., Verdugo T., 2007, *New Journal of Physics*, **9**, 447
- Kneib J. P., Mellier Y., Fort B., Mathez G., 1993, *A&A*, **273**, 367
- Kumar R., Carroll C., Hartikainen A., Martin O., 2019, *Journal of Open Source Software*, **4**, 1143
- Li R., et al., 2016, *MNRAS*, **458**, 2573
- Limousin M., Beauchesne B., Jullo E., 2022, *A&A*, **664**, A90
- Lu S., Zhu K., Cappellari M., Li R., Mao S., Xu D., 2024, *MNRAS*, **530**, 4474
- Mahler G., et al., 2023, *ApJ*, **945**, 49
- Mehrgan K., Thomas J., Saglia R., Parikh T., Neureiter B., Erwin P., Bender R., 2024, *ApJ*, **961**, 127
- Montes M., Trujillo I., 2019, *MNRAS*, **482**, 2838
- Moster B. P., Naab T., White S. D. M., 2013, *MNRAS*, **428**, 3121
- Newman A. B., Treu T., Ellis R. S., Sand D. J., 2013, *ApJ*, **765**, 25
- Niemiec A., et al., 2017, *MNRAS*, **471**, 1153
- Niemiec A., Jullo E., Giocoli C., Limousin M., Jauzac M., 2019, *MNRAS*, **487**, 653
- Niemiec A., Giocoli C., Cohen E., Jauzac M., Jullo E., Limousin M., 2022, *MNRAS*, **512**, 6021
- Nightingale J., et al., 2021, *The Journal of Open Source Software*, **6**, 2825
- Oldham L., Auger M., 2018, *MNRAS*, **474**, 4169
- Pedregosa F., et al., 2011, *Journal of Machine Learning Research*, **12**, 2825
- Pillepich A., et al., 2018, *MNRAS*, **473**, 4077
- Posacki S., Cappellari M., Treu T., Pellegrini S., Ciotti L., 2015, *MNRAS*, **446**, 493
- Robertson A., Massey R., Eke V., Schaye J., Theuns T., 2021, *MNRAS*, **501**, 4610
- Salpeter E. E., 1955, *ApJ*, **121**, 161
- Schwarz G., 1978, *Ann. Statist.*, **6**, 461
- Shajib A. J., Treu T., Birrer S., Sonnenfeld A., 2021, *MNRAS*, **503**, 2380
- Sharma S., Richard J., Yuan T., Patrício V., Kewley L., Rigby J. R., Gupta A., Leethochawalit N., 2021, *MNRAS*, **505**, L1
- Sifón C., et al., 2015, *MNRAS*, **454**, 3938
- Sifón C., Herbonnet R., Hoekstra H., van der Burg R. F. J., Viola M., 2018, *MNRAS*, **478**, 1244
- Simon D. A., Cappellari M., Hartke J., 2024, *MNRAS*, **527**, 2341
- Sirks E. L., Oman K. A., Robertson A., Massey R., Frenk C., 2022, *MNRAS*, **511**, 5927
- Smith R. J., 2020, *ARA&A*, **58**, 577
- Spearman C., 1904, *The American Journal of Psychology*, **15**, 72
- Tortorelli L., et al., 2018, *MNRAS*, **477**, 648
- Wang C., et al., 2024, *MNRAS*, **528**, 2728
- Watanabe S., 2010, arXiv e-prints, p. [arXiv:1004.2316](https://arxiv.org/abs/1004.2316)
- Weinberger R., et al., 2017, *MNRAS*, **465**, 3291
- Wright A. H., et al., 2017, *MNRAS*, **470**, 283
- Zhao H., 1996, *MNRAS*, **278**, 488
- van den Bosch R. C. E., 2016, *ApJ*, **831**, 134

## APPENDIX A: MASS MODEL PARAMETERS AND POSTERIOIRS

In this appendix, we present the model posteriors for the three models with a “BCG - ML 2” parametrisation. The 1D posterior distribu-

tions of each model parameter are presented in Fig. A1, Fig. A2 and Fig. A3. It shows the models with a delayed SFH, a double power-law SFH and the LEPHARE SED model, respectively. In our optimisation procedure detailed in Sect. 3.5, we use three different distributions that are presented in different colours. To speed up the inference process, we use a first approximation of the posterior based on a multivariate normal distribution, shown in blue. We use the 1D posterior of this multivariate to transform our parameter space to increase the volume represented by the model posteriors with respect to the priors. The posteriors obtained by the nested sampling runs are presented in red. In this run, parameters are not constrained by the BCG & ICL kinematics. The last distribution presented in green is the final approximation of the posterior obtained after the importance sampling step to incorporate the BCG & ICL constraints.

We are presenting tabulated values of each parameter with their  $1\sigma$  CI and best-fitting values in Table A1, Table A2 and Table A3. These are associated with the models having a delayed SFH, a double power-law SFH or LEPHARE SED model, respectively.

This paper has been typeset from a  $\text{\LaTeX}$  file prepared by the author.

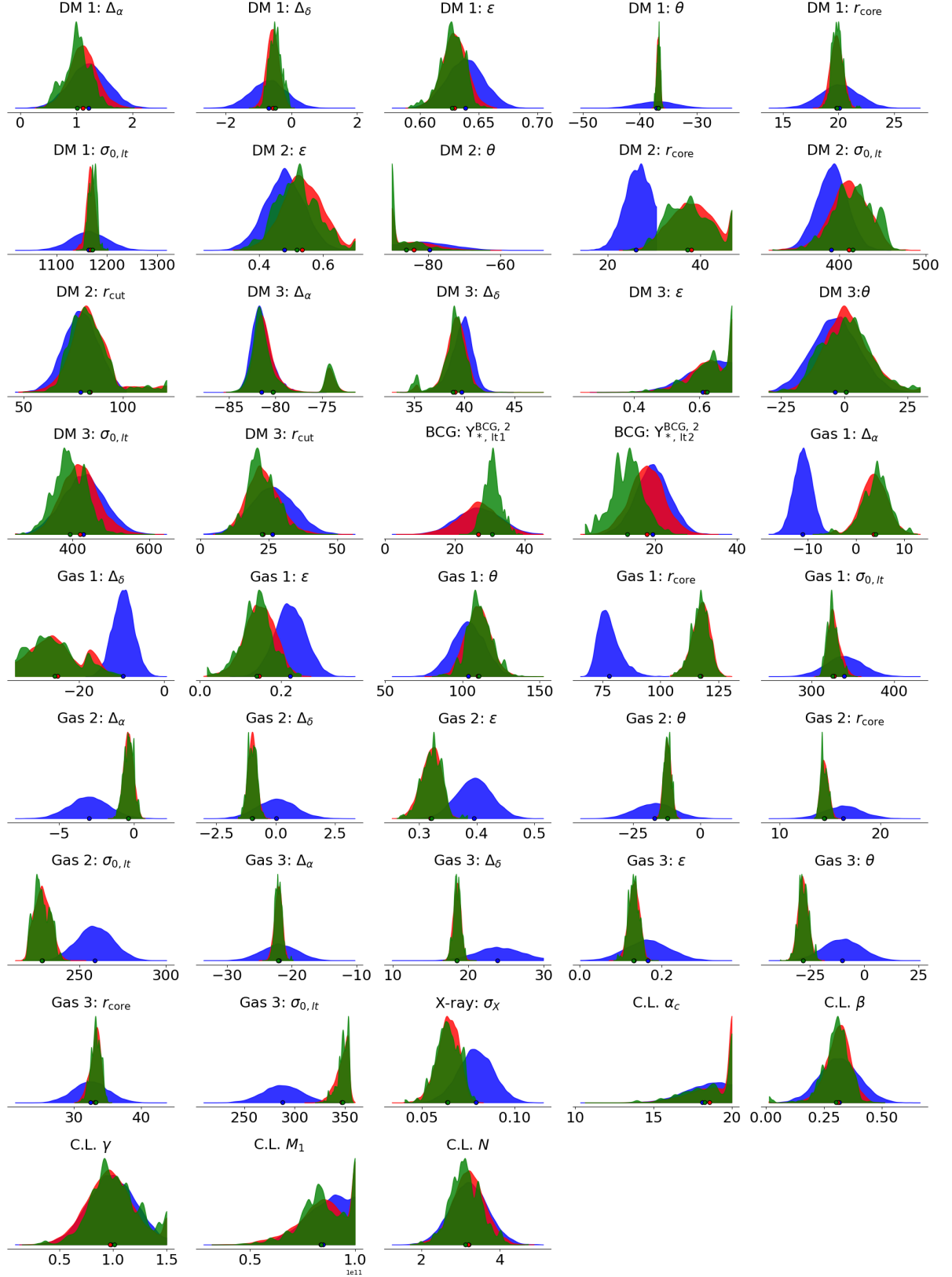


**Figure A1.** 1D posterior density of each model parameter. The model considered here has a “BCG - ML 2” parametrisation and the delayed SFH model. Each colour represents the distribution at a different step of our optimisation process as detailed in Sect. 3.5. The blue distribution represents the initial approximation based on a multivariate normal distribution. The red and green posteriors show the biased and final approximate posteriors or the distributions before and after the importance sampling step. dPIEs parameters are presented with the relative x-coordinate  $\Delta_\alpha$  (arcsec), the relative y-coordinate  $\Delta_\delta$  (arcsec), ellipticity  $\epsilon$ , position angle  $\theta$  (degree), core radius  $r_{\text{core}}$  (arcsec), cut radius  $r_{\text{cut}}$  (arcsec) and central velocity dispersion  $\sigma_{0,lt}$  (km/s). For the BCG & ICL component, only its normalisation ( $\gamma_{*,lt,1/2}^{\text{BCG},2}$ ) is presented. The cluster member parameters are shown by the spatial scale,  $\alpha_c$ , the power-law slopes,  $\delta$  and  $\gamma$ , the turn-off mass,  $M_1$  ( $M_\odot$ ), and the normalisation,  $N$ .

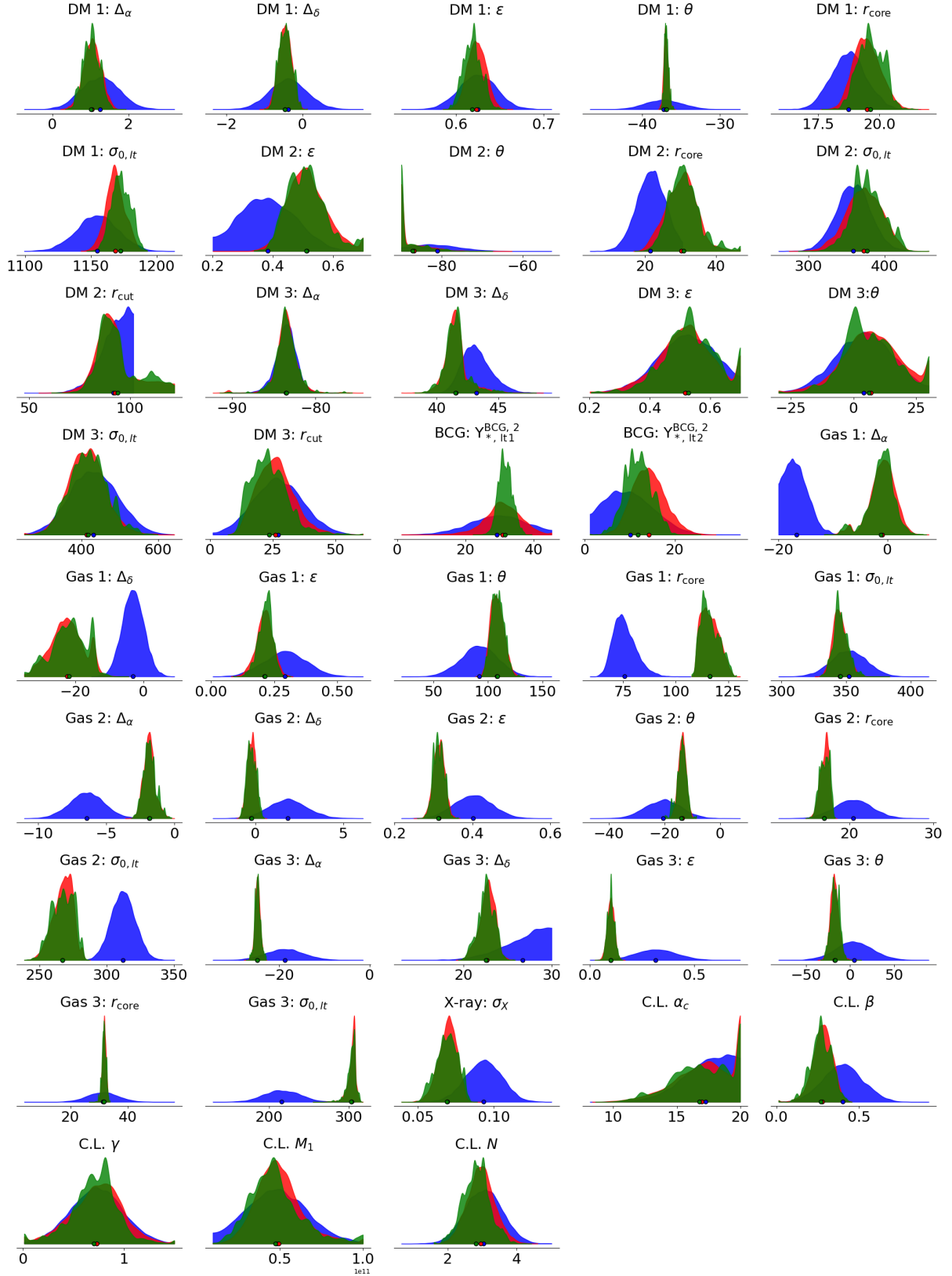


**Figure A2.** Same as Fig. A1 for the model with the double power-law SFH.

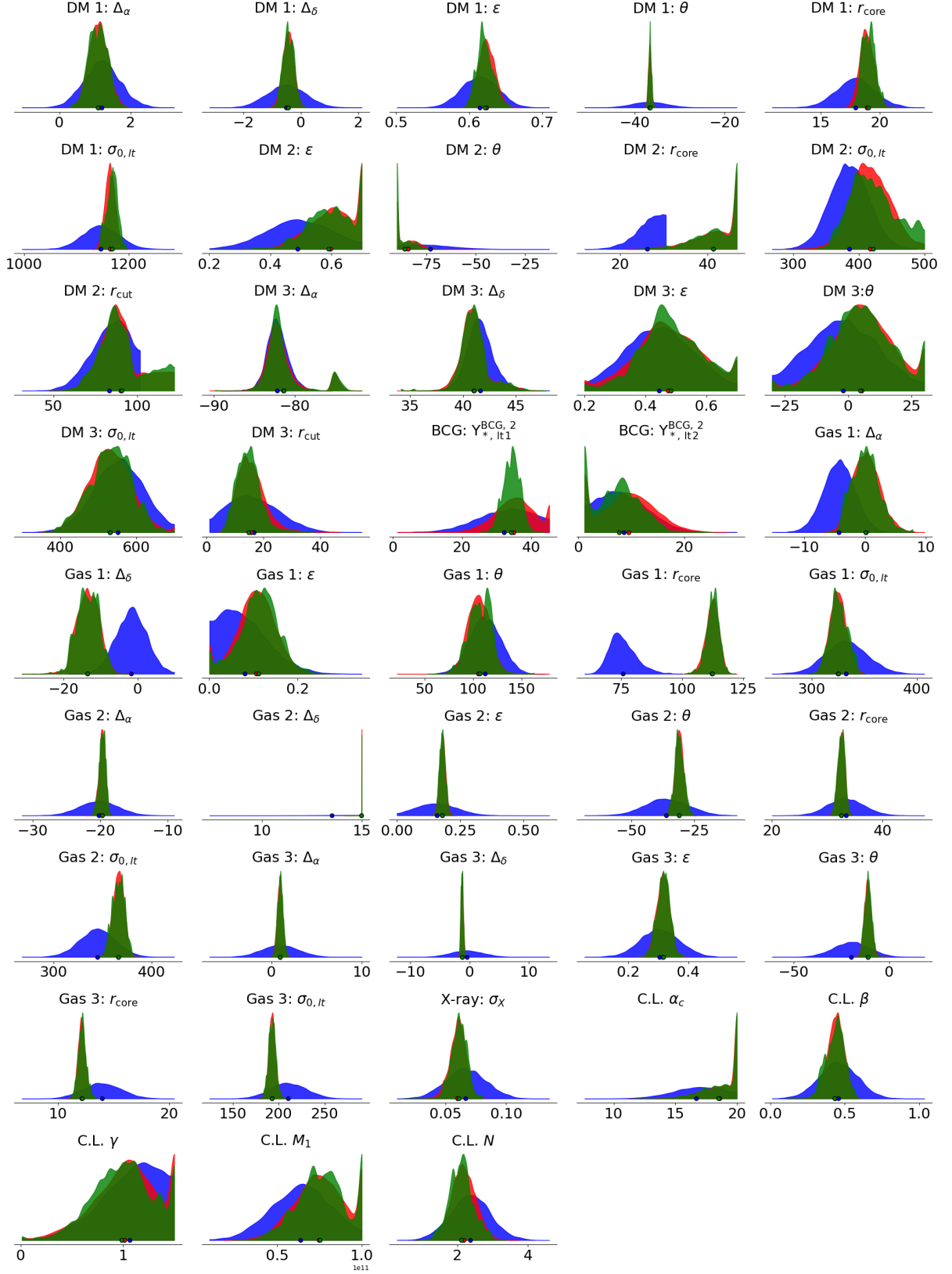


Figure A3. Same as Fig. A1 for the model with LEPHARE SED model.

ID	$\Delta\alpha$ kpc	$\Delta\delta$ kpc	$\phi$ degree	$\epsilon$
DM-main	$4.9^{+1.1}_{-1.2}$ (4.9)	$-2.4^{+0.9}_{-0.9}$ (-2.7)	$-36.7^{+0.2}_{-0.3}$ (-36.9)	$0.627^{+0.01}_{-0.009}$ (0.627)
DM-BCG	[0.0]	[0.0]	$-87.4^{+5.9}_{-2.5}$ (-89.9)	$0.518^{+0.063}_{-0.066}$ (0.641)
DM-NE	$-400.9^{+34.2}_{-3.7}$ (-391.7)	$192.1^{+4.6}_{-5.6}$ (189.3)	$0.6^{+9.2}_{-9.8}$ (16.3)	$0.633^{+0.056}_{-0.07}$ (0.641)
Gas-1	$21.1^{+11.8}_{-14.8}$ (23.9)	$-130.6^{+39.8}_{-25.4}$ (-171.1)	$110.0^{+8.6}_{-6.7}$ (118.6)	$0.141^{+0.033}_{-0.036}$ (0.145)
Gas-2	$-1.6^{+1.5}_{-1.8}$ (-2.1)	$-4.9^{+0.9}_{-0.9}$ (-4.1)	$-12.2^{+1.3}_{-1.3}$ (-11.3)	$0.323^{+0.015}_{-0.02}$ (0.328)
Gas-3	$-108.9^{+2.8}_{-2.4}$ (-107.8)	$90.9^{+2.4}_{-2.1}$ (94.9)	$-28.2^{+2.6}_{-2.1}$ (-28.5)	$0.13^{+0.013}_{-0.012}$ (0.118)

ID	$r_{\text{core}}$ kpc	$r_{\text{cut}}$ kpc	$\sigma_{0,\text{lt}}$ km/s
DM-main	$97.6^{+2.4}_{-2.2}$ (95.5)	[3000]	$1171^{+7}_{-8}$ (1179)
DM-BCG	$182.9^{+24.4}_{-22.4}$ (174.0)	$401^{+45}_{-38}$ (394)	$416^{+23}_{-23}$ (377)
DM-NE	[2.5]	$107^{+31}_{-21}$ (102)	$391^{+44}_{-38}$ (410)
Gas-1	$576.7^{+16.4}_{-20.3}$ (600.6)	[1250]	$324^{+7}_{-6}$ (318)
Gas-2	$70.5^{+2.2}_{-1.4}$ (72.0)	[1250]	$227^{+5}_{-4}$ (232)
Gas-3	$163.7^{+3.9}_{-3.5}$ (169.1)	[1250]	$348^{+4}_{-5}$ (353)

ID	$\Upsilon_{*,\text{lt } 1}^{\text{BCG}, 2}$	$\Upsilon_{*,\text{lt } 2}^{\text{BCG}, 2}$
BCG	$30.58^{+2.34}_{-2.35}$ (35.27)	$13.44^{+3.35}_{-3.68}$ (8.11)

ID	$\alpha_c$	$\delta$	$\gamma$	$M_1$ $10^{10} M_{\odot}$	$N$
Gal.	$18.51^{+1.48}_{-1.69}$ (16.41)	$0.3^{+0.04}_{-0.05}$ (0.23)	$0.99^{+0.25}_{-0.19}$ (0.9)	$8.38^{+1.17}_{-0.92}$ (8.14)	$3.1^{+0.39}_{-0.36}$ (3.07)

**Table A1.** Model parameters distributions of each mass component for the model with a “BCG - ML 2” parametrisation and the delayed SFH model. Starting from the top, the first two tables present the mass component modelled with dPIEs, the third table shows the MGE component, and the last one shows the cluster member population parameters. Each parameter is represented as median<sup>84 per cent limit</sup><sub>16 per cent limit</sub> (best-fit) except the ones fixed a priori that are shown in brackets.  $\Delta\alpha$  and  $\Delta\delta$  are the coordinates of dPIE haloes relative to the BCG centre at  $\alpha(\text{J2000}) = 342.183213$  and  $\delta(\text{J2000}) = -44.530897$ . The lt label refers to the velocity dispersions of dPIEs as implemented in LENSTOOL.

ID	$\Delta\alpha$ kpc	$\Delta\delta$ kpc	$\phi$ degree	$\epsilon$
DM-main	$5.0^{+1.1}_{-1.1}$ (5.4)	$-2.2^{+0.8}_{-0.8}$ (-3.2)	$-36.9^{+0.2}_{-0.2}$ (-36.6)	$0.618^{+0.01}_{-0.01}$ (0.632)
DM-BCG	[0.0]	[0.0]	$-88.8^{+5.3}_{-1.1}$ (-89.9)	$0.506^{+0.064}_{-0.057}$ (0.612)
DM-NE	$-411.2^{+5.6}_{-4.8}$ (-407.1)	$204.2^{+3.1}_{-3.5}$ (219.7)	$5.0^{+11.2}_{-8.0}$ (17.4)	$0.528^{+0.085}_{-0.08}$ (0.628)
Gas-1	$-4.7^{+8.7}_{-11.3}$ (-18.3)	$-106.3^{+28.2}_{-25.5}$ (-101.6)	$108.4^{+6.3}_{-5.5}$ (102.7)	$0.216^{+0.022}_{-0.03}$ (0.197)
Gas-2	$-9.1^{+2.3}_{-2.1}$ (-10.8)	$-1.1^{+1.4}_{-1.2}$ (-0.1)	$-13.7^{+1.4}_{-1.7}$ (-14.2)	$0.312^{+0.014}_{-0.013}$ (0.311)
Gas-3	$-122.2^{+3.1}_{-2.8}$ (-125.1)	$111.0^{+4.7}_{-4.4}$ (110.7)	$-17.1^{+4.8}_{-4.9}$ (-21.0)	$0.1^{+0.016}_{-0.017}$ (0.095)

ID	$r_{\text{core}}$ kpc	$r_{\text{cut}}$ kpc	$\sigma_{0,\text{lt}}$ km/s
DM-main	$96.5^{+2.9}_{-2.5}$ (94.7)	[3000]	$1172^{+8}_{-6}$ (1170)
DM-BCG	$150.5^{+20.6}_{-19.1}$ (167.4)	$448^{+76}_{-30}$ (454)	$376^{+22}_{-18}$ (396)
DM-NE	[2.5]	$112^{+35}_{-32}$ (111)	$416^{+49}_{-48}$ (420)
Gas-1	$568.8^{+27.5}_{-17.5}$ (569.6)	[1250]	$345^{+5}_{-4}$ (345)
Gas-2	$83.8^{+2.9}_{-3.3}$ (83.9)	[1250]	$267^{+8}_{-9}$ (268)
Gas-3	$155.8^{+3.6}_{-3.3}$ (157.5)	[1250]	$304^{+3}_{-5}$ (301)

ID	$\Upsilon_{*,\text{lt } 1}^{\text{BCG}, 2}$	$\Upsilon_{*,\text{lt } 2}^{\text{BCG}, 2}$
BCG	$31.56^{+2.19}_{-1.99}$ (31.31)	$11.73^{+3.22}_{-2.87}$ (11.49)

ID	$\alpha_c$	$\delta$	$\gamma$	$M_1$ $10^{10} M_{\odot}$	$N$
Gal.	$16.87^{+2.25}_{-2.24}$ (17.92)	$0.26^{+0.06}_{-0.06}$ (0.24)	$0.71^{+0.18}_{-0.22}$ (0.83)	$4.58^{+1.54}_{-1.3}$ (3.68)	$2.82^{+0.35}_{-0.4}$ (3.01)

**Table A2.** Same as Table A1 for the model with the double power-law SFH.

ID	$\Delta\alpha$ kpc	$\Delta\delta$ kpc	$\phi$ degree	$\epsilon$
DM-main	$5.3^{+1.2}_{-1.3} (4.3)$	$-2.1^{+0.9}_{-0.9} (-1.5)$	$-36.6^{+0.3}_{-0.3} (-36.6)$	$0.62^{+0.012}_{-0.009} (0.623)$
DM-BCG	[0.0]	[0.0]	$-87.4^{+6.5}_{-2.5} (-84.1)$	$0.595^{+0.075}_{-0.073} (0.555)$
DM-NE	$-404.2^{+9.6}_{-4.9} (-370.7)$	$201.5^{+5.1}_{-4.8} (195.2)$	$4.6^{+12.4}_{-11.5} (6.6)$	$0.474^{+0.112}_{-0.087} (0.403)$
Gas-1	$0.1^{+10.6}_{-11.3} (-17.4)$	$-66.5^{+14.6}_{-14.7} (-69.8)$	$107.1^{+11.1}_{-11.9} (114.7)$	$0.113^{+0.038}_{-0.043} (0.122)$
Gas-2	$-96.8^{+2.3}_{-2.4} (-92.9)$	$73.8^{+0.0}_{0.0} (73.8)$	$-31.0^{+2.0}_{-1.5} (-29.4)$	$0.179^{+0.011}_{-0.011} (0.188)$
Gas-3	$4.7^{+1.3}_{-1.5} (3.0)$	$-6.3^{+0.9}_{-0.9} (-6.5)$	$-11.1^{+1.8}_{-1.8} (-11.2)$	$0.316^{+0.02}_{-0.022} (0.32)$

ID	$r_{\text{core}}$ kpc	$r_{\text{cut}}$ kpc	$\sigma_{0,\text{lt}}$ km/s
DM-main	$93.7^{+2.6}_{-2.8} (90.3)$	[3000]	$1168^{+9}_{-11} (1160)$
DM-BCG	$206.8^{+23.3}_{-27.7} (216.9)$	$432^{+98}_{-49} (520)$	$417^{+42}_{-30} (426)$
DM-NE	[2.5]	$71^{+19}_{-19} (50)$	$534^{+49}_{-59} (501)$
Gas-1	$554.3^{+11.2}_{-13.2} (559.9)$	[1250]	$325^{+9}_{-7} (333)$
Gas-2	$160.0^{+3.0}_{-3.3} (158.4)$	[1250]	$366^{+6}_{-6} (363)$
Gas-3	$59.9^{+1.7}_{-1.7} (58.8)$	[1250]	$192^{+3}_{-3} (191)$

ID	$\Upsilon_{*,\text{lt}1}^{\text{BCG},2}$	$\Upsilon_{*,\text{lt}2}^{\text{BCG},2}$
BCG-1	$34.45^{+2.29}_{-2.63} (34.43)$	$7.8^{+3.94}_{-4.76} (1.6)$

ID	$\alpha_c$	$\delta$	$\gamma$	$M_1$ $10^{10} M_{\odot}$	$N$
Gal.	$18.85^{+1.13}_{-1.83} (17.32)$	$0.43^{+0.05}_{-0.07} (0.36)$	$0.99^{+0.29}_{-0.29} (0.85)$	$7.56^{+1.28}_{-1.4} (8.39)$	$2.1^{+0.31}_{-0.31} (2.72)$

**Table A3.** Same as Table A1 for the model with LePHARE SED model.